Archives of Civil and Mechanical Engineering (2021) 21:6
https://doi.org/10.1007/s43452-020-00150-x

ORIGINAL ARTICLE

Free vibration and buckling analyses of FG porous sandwich curved microbeams in thermal environment under magnetic field based on modified couple stress theory

Ehsan Arshid[1] · Hossein Arshid[2] · Saeed Amir[1] · S. Behnam Mousavi[1]

Received: 26 May 2020 / Revised: 21 October 2020 / Accepted: 19 November 2020 / Published online: 2 January 2021

Abstract

Porous sandwich structures include different numbers of layers and are capable of demonstrating higher values of strength to weight ratio in comparison with traditional sandwich structures. Free vibration and mechanical buckling responses of a three-layered curved microbeam was investigated under the Lorentz magnetic load in the current study. A viscoelastic substrate was considered and the effect of the thermal environment on its mechanical properties was assessed. The core was composed of the functionally graded porous materials whose properties changed across the thickness based on some given functions. The face sheets were FG-carbon nanotube-reinforced composites and the influence of the placement of CNTs was evaluated on the behavior of the faces. Using the extended rule of mixture, their effective properties were determined. Modified couple stress theory was used to predict the results in the micro-dimension. While the governing equations were derived based on the higher order shear deformation theory and energy method, and mathematically solved via Navier's method. The results were validated with the previously published works, considering the effects of various parameters. As comprehensively explained in the results section, natural frequencies and critical buckling loads were reduced by enhancing the central opening angle. Moreover, an increase in the porosity coefficient declined the mentioned values, but increasing the CNTs content showed the opposite effect. The outcomes of this study may help in the design and manufacturing of various equipment using such smart structures, making high stiffness to weight ratios more accessible.

Keywords Curved microbeams · Modified couple stress theory · Porous materials · Carbon nanotube-reinforced composites · Sandwich structures · Lorentz magnetic load

1 Introduction

Sandwich structures are often three-layered structures whose core (central layer) is integrated with two skins. Usually, the core has a lower strength in comparison with the face sheets. Porous materials are often used as core. The idea behind the development of such structures is the high demand of different industries for structures with low weight-to-strength ratios as the most important characteristics of sandwich structures. The extensive applications of porous materials in different fields have encouraged the researchers to further investigate them. For example, metal foams, a class of porous materials, have found wide applications in industries such as vehicles, high-speed trains, energy, and vibration absorbers (Fig. 1). Composites are multi-component materials whose properties are generally better than their components. Each composite consists of a matrix phase and one or more reinforcement phases. It should be noted that the components of a composite do not chemically merge as they fully maintain their chemical and natural properties; thus creating a definite common interface between the components [1]. Composites have several advantages, leading to their wide applications nowadays. Polymeric nanocomposites may be used in fuel tanks and tubes, military industries, automobile industries, marine structures, construction industry, sports equipment, and medical equipment [2]. Some of these applications are shown in Fig. 2. In recent years, nanotubes have been developed and applied by the rapid

✉ Saeed Amir
samir@kashanu.ac.ir; saeid_amir27111@yahoo.com

1 Department of Solid Mechanics, Faculty of Mechanical Engineering, University of Kashan, Kashan, Iran

2 Department of Mechanical Engineering, Qom Branch, Islamic Azad University, Qom, Iran

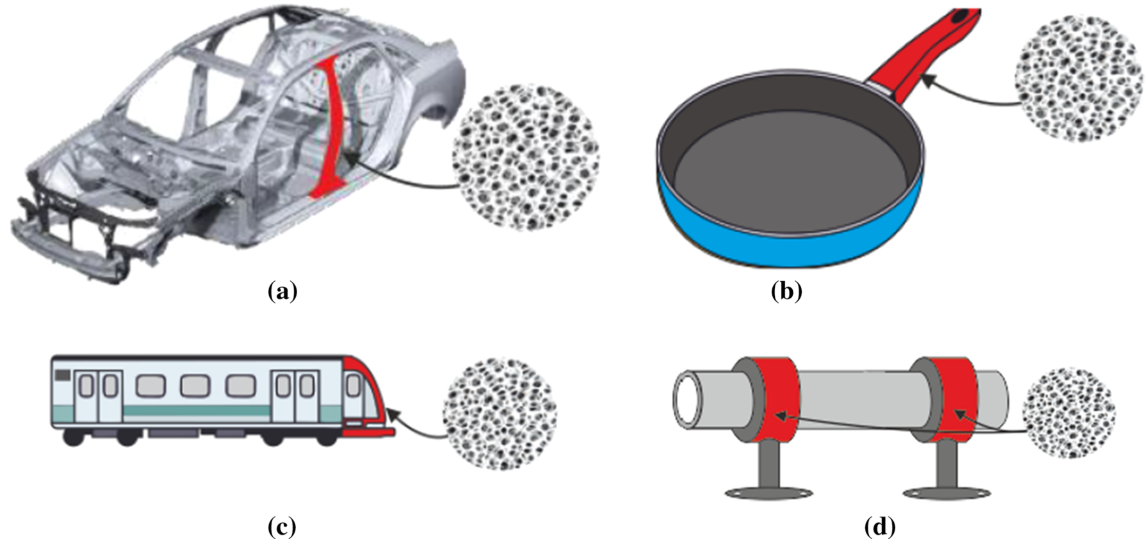

Fig. 1 Some of porous materials applications in different areas such as **a** frame/substructure of some cars; **b** kitchen pots and pans; **c** trains; **d** vibration absorbers in pipes

Fig. 2 Some of polymer nanocomposites applications

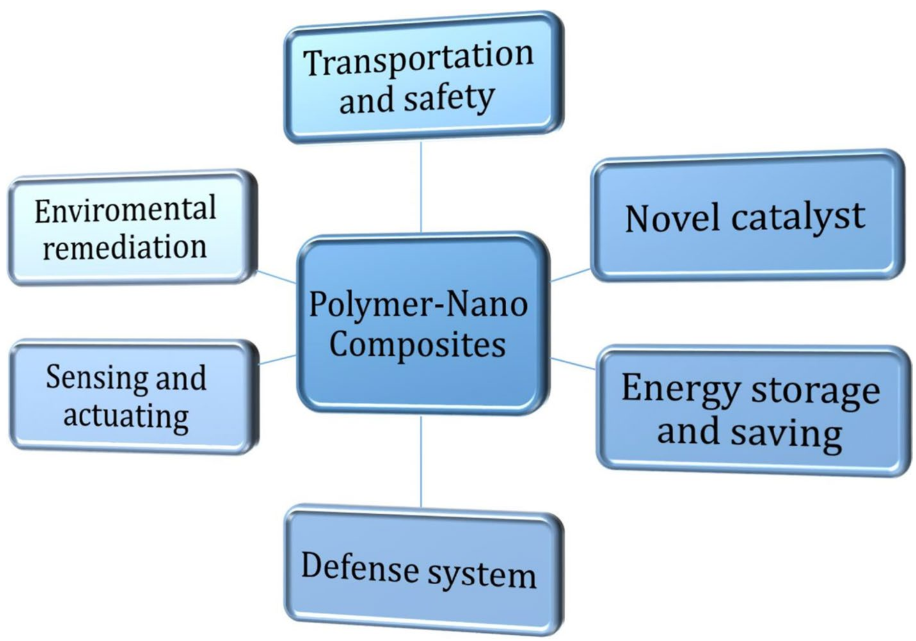

advancement in science and technology. In the past 2 decades, their usage has been accelerated with the advent of carbon nanotubes (CNTs) by Iijima [3]. CNTs have unique mechanical, magneto-electrical, and chemical properties. High rigidity and stiffness-to-weight ratio, electrical conductivity, and high-temperature strength are among some of their characteristics [4]. CNTs have been used as reinforcement of composites and significantly improved their properties. CNTs are divided into single-walled and multi-walled types. Single-walled carbon nanotubes (SWCNTs) consist of a simple structure. Some prediction suggests that SWCNTs can be conductive or semiconductor [5]. Its electrical conductivity depends on the exact geometry of carbon atoms. Based on the arrangement of the carbon atoms, SWCNTs are also divided into three major categories. Mechanical analysis of CNT-reinforced composites (CNTRCs) was presented by various researchers. Thostenson and Chou [6] modeled the elastic properties of CNTRCs in 2003. They investigated the effect of the size and structure of CNTs based on the elastic characteristics of the composite matrix. The bending behavior of a CNT-reinforced composite plate between two piezoelectric layers was investigated by Alibeigloo [7] under a uniform mechanical load. Duc et al. [8] considered thermal and mechanical stability of FG-CNTRC truncated conical shells. They used classical shells theory and Galerkin method to obtain the results and considered the effect of the most important variants such as semi-vertex angle and elastic medium on the linear thermal and mechanical buckling load. Shariati et al. [9] presented their study on the large-amplitude nonlinear vibrations in multi-sized hybrid nanocomposites disk rested on nonlinear elastic media and located in an environment whose temperature was gradually changed.

Many researchers have tried to investigate different types of sandwich structures with diverse theories, so far. One of them is a study by Khatua and Cheung [10] dated 1973 which addressed the bending and vibration behaviors of multilayer beams and plates. After that, Maheri and Adams [11] studied this topic and published the results of their study on the flexural vibration damping of honeycomb sandwich beams in 1992. Furthermore, transverse vibrations of a fluid-saturated thin rectangular porous plate were explored by Leclaire et al. [12] in 2001. Takahashi and Tanaka [13] investigated the flexural vibration of perforated plates and porous elastic materials under acoustic loads in 2002. Elastic buckling and static bending of shear deformable functionally graded (FG) porous beams were examined by Chen et al. [14]. As another paper, shock-absorbing characteristics and vibration transmissibility of honeycomb paperboard were studied by Yanfeng and Jinghui [15]. Ait Atmane et al. [16] studied the effect of thickness stretching and porosity on the mechanical response of FG beams. In another work, the vibrational behavior of shear deformable FG porous beams was estimated by Chen et al. [17] in both free and forced cases. More recently, Katunin [18], published an article about honeycomb sandwich structures and used wavelet analysis to consider the vibration-based spatial damage identification. After that, nonlinear free vibration and post-buckling behaviors of multilayer FG porous nanocomposite beams were evaluated by Chen et al. [19]. They used Graphene platelets (GPLs)-reinforced metal foams and indicated the essential role of the GPLs volume fraction in enhancing the stiffness of the structure. Moreover, they found the structure's vibration and post-buckling performances were affected by the pore and GPL distribution types. Furthermore, in 2017, Duc et al. [20] hired the first-order shear deformation theory (FSDT) to study the vibration of sandwich composite cylindrical panels with an auxetic honeycomb core. They employed von Karman strain–displacement relations and Airy stress functions method to derive the equations and solved them using Galerkin and fourth-order Runge–Kutta methods. In 2018, Amir et al. [21] addressed the buckling behavior of sandwich plates considering the flexoelectricity effect. In another work, they investigated a similar effect but on the vibrational response of nanocomposite sandwich plates [22]. Besides this, nonlinear vibration of sandwich beams with entangled cross-linked fibers core was examined by Piollet et al. [23]. They compared two sandwich beams with the reference honeycomb beams. Safarpour et al. [24] assessed the frequency characteristics of GPL-reinforced composite viscoelastic thick annular plate with the aid of generalized differential quadrature method. Furthermore, Babaei et al. [25] investigated the thermal buckling and post-buckling responses of FG porous beams with geometrical imperfection. Kumar and Renji [26] conducted a profound study on composite honeycomb sandwich panels exposed to the diffusive acoustic field in a reverberation chamber in 2019 and succeed to measure the strains. The extended rule of mixture (ERM) and Halpin–Tsai micromechanical models were used by Moayedi et al. [27] to investigate the buckling and frequency responses of a GPL-reinforced composite microdisk.

Regarding different behaviors of structures in macro and small dimensions, and also due to the extensive application of small-scale structures (e.g. nano- and microbeams, plates, and shells) in measuring equipment, medicine, and industries, the researchers were encouraged to analyze the mechanical properties in small scales [28]. One of the first studies was conducted by Eringen who presented the nonlocal theory to evaluate the structures in the nanoscale [29, 30]. Earlier, small scales' effects consideration extended rapidly by numerous authors. Amir et al. [31] used the modified couple stress theory (MCST) to capture the size effect for analyzing a sandwich beam with a porous core. In another study, Amir et al. [32] considered the size-dependent vibrational behavior of a three-layered nanoplate based on Eringen's nonlocal elasticity theory. The effects of agglomerated CNTs as reinforcement on the size-dependent vibration of embedded curved microbeams based on MCST investigated by Allahkarami and Nikkhah-Bahrami [33]. Alipour and Shariyat [34] used nonlocal zigzag analytical solution for Laplacian hygrothermal stress analysis of annular sandwich macro/nanoplates with poor adhesions and FG porous cores. Also, a study conducted by Yi et al. [35] on size-dependent large-amplitude free oscillations of FG porous nanoshells incorporating vibrational mode interactions. A size-dependent exact theory was presented by Safarpour et al. [36] to analyze the thermal buckling and free and forced vibration of a temperature-dependent FG multilayer GPLs-reinforced composite nanostructure. The influence of modified strain gradient theory (MSGT) was investigated by Esmailpoor Hajilak et al. [37] on buckling, free and forced vibration characteristics of the GPL-reinforced composite cylindrical nanoshell in a thermal environment. As stated, their study was based on MSGT which suggested three material length-scale parameters (i.e. two parameters more than MCST). Earlier in 2020, Sobhy [38] used the differential quadrature method to evaluate the bending in three types of FG sandwich curved beams with honeycomb core in polar coordinate. He investigated magneto-hygrothermal effects on the deflection of the mentioned under consideration structure. In another paper, dynamic behaviors of the FG porous beams were presented by Lei et al. [39] under flexible boundary constraints. They examined two types of single- and multi-span beams.

Numerous theories have been developed to analyze the structures such as beams, plates, and shells; some of them consider the shear deformation effects while others neglected that. The theories accounting for these effects, especially those considering higher order functions, have found wide applications these days. First- and third-order, parabolic, trigonometric, and quasi-3D functions can be mentioned as the prominent higher order shear deformation theories. For example, Omidi Bidgoli et al. [40] used the FSDT to analyze the thermoelastic behavior of FGM rotating cylinders resting on a friction bed which was subjected to a thermal gradient and an external torque. This theory (i.e. FSDT) was also used by Mahani et al. [41] to consider thermal buckling of laminated nanocomposite conical shell reinforced with GPLs. Recently, Arshid et al. [42] took the shear deformation into account by employing the FSDT to investigate the static behavior of a three-layered sandwich circular microplate. Bousahla et al. [43] investigated the buckling and vibrational behaviors of the composite beam armed with SWCNTs resting on the Winkler-Pasternak elastic foundation. The CNTRCs beam was modeled by a novel integral FSDT. Also, hygrothermal and mechanical buckling responses of simply supported FG sandwich plates were investigated by a novel shear deformation theory in the study of Refrafi et al. [44]. Their model took into consideration the shear deformation effects and ensures the zero shear stresses on the free surfaces of the FG sandwich plate without requiring the correction factors. Moreover, a novel four-unknown integral model was introduced by Chikr et al. [45] for the buckling response of FG sandwich plates under various boundary conditions using Galerkin's approach.

A review of the aforementioned studies shows the absence of a comprehensive study on vibrational and buckling characteristics of sandwich curved microbeams using higher order shear deformation theory (HSDT). Although there are some works about FG structures, no study has addressed the static and dynamic behaviors of a three-layer microstructure including an FG porous core and two nanocomposite face sheets. Therefore, the current paper aims to investigate the mechanical buckling and vibrational behavior of a sandwich curved microbeam placed on the visco-Pasternak substrate in a thermal environment. Also, the influence of the Lorentz magnetic load was investigated on the static and dynamic responses. Various patterns of CNTs' dispersion were considered in this work, and the effective thermo-mechanical properties of the face sheets were determined via the ERM due to its simplicity and accuracy. By employing the extended Hamilton's principle and variational formulation, the governing equations were derived, and since the classical elasticity theory does not consider the influence of dimension, the MCST was employed to capture the size effect. Navier's solution method was used to analytically solve the differential equations system. Based on the results, it is possible to design and manufacture various equipment using such smart structures making the high stiffness to weight ratio more accessible than before.

2 Mathematical formulation

2.1 Geometry

As stated in the previous section, the studied curved microbeam is composed of three layers, as shown in Fig. 3. The core was made from FG porous materials, while the skins were made from FG-CNTRCs. The curvature radius and length are presented by R and L, respectively. The central opening angle is denoted by θ, and the thicknesses of the

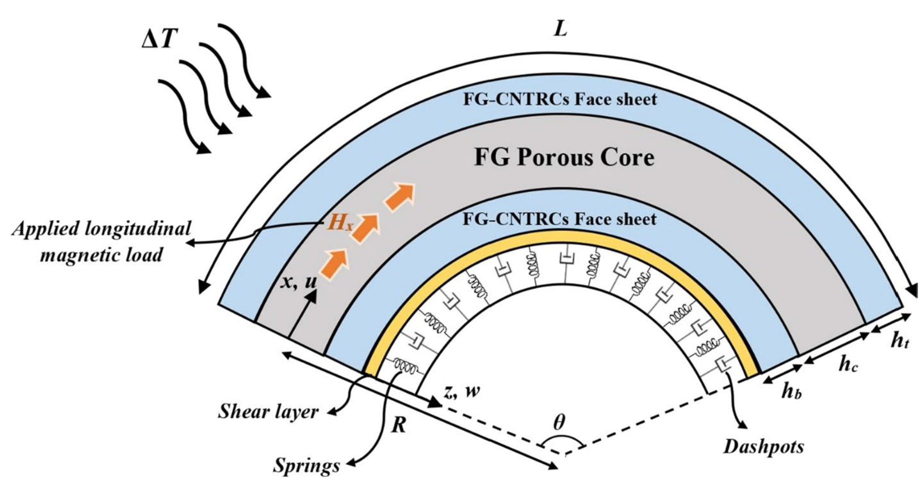

Fig. 3 Schematic of the sandwich curved micro beam under magnetic load effect resting on viscoelastic substrate in thermal environment

layers from the bottom to the top are specified with h_b, h_c, and h_t, respectively. The effect of the Lorentz magnetic force was considered as a body force influencing the mechanical behavior of the structure. Moreover, the structure is located on a three-parameter viscoelastic substrate, which includes springs, shear layer, and dashpots. The thermo-mechanical properties of all three layers changed through their thicknesses according to some given functions; they also varied by temperature variations. The Cartesian coordinate system was selected to analyze the microstructure whose origin locates on the left corner of the mid-layer.

2.2 Constitutive law

The general stress–strain relations in the thermal environment for all layers of the curved microbeam can be demonstrated as follows [46]:

$$\begin{Bmatrix} \sigma^i_{xx} \\ \sigma^i_{xz} \end{Bmatrix} = \begin{bmatrix} Q^i_{11} & 0 \\ 0 & Q^i_{55} \end{bmatrix} \begin{Bmatrix} \varepsilon_{xx} - \alpha^i_{11}\Delta T \\ 2\varepsilon_{xz} \end{Bmatrix}, \quad i = t, c, b \tag{1}$$

in which σ_{xj} and ε_{xj} ($j = x, z$) are the stress and strain components, respectively. α_{11} shows the thermal expansion coefficient, and ΔT represents the temperature variations relative to the ambient temperature. It should be noted that i superscript denotes each layer, namely top, core, and bottom. Also, Q_{11} and Q_{55} are the components of the stiffness matrix which can be separately defined for each layer:

2.2.1 FG porous core

The components of the stiffness matrix of the FG porous core can be determined through the below relations [47]:

$$Q_{11} = \frac{E(z)}{1 - \nu^2}, \qquad Q_{55} = G(z) = \frac{E(z)}{2(1 + \nu)} \tag{2}$$

where ν is the Poisson's ratio, and $E(z)$ is Young's elasticity modulus, which depends on thickness. The mechanical properties of the porous core are graded functionally across its thickness based on three different patterns, called the porosity distributions. These patterns show the pore's placement in the core. The elasticity modulus and density variations through the core's thickness can be generally introduced as:

$$\begin{aligned} E(z) &= E_1 f(z) \\ \rho(z) &= \rho_1 g(z), \end{aligned} \tag{3}$$

where E_1 and ρ_1 are the maximum values of Young's modulus and density, respectively. Also, $f(z)$ and $g(z)$ show the porosity functions specified for each pattern as follows:

Type A: In this type of porosity distribution, the pores are asymmetrically placed with respect to the mid-plane of the core. Therefore, the porosity functions are defined using a cosine pattern as follows [48]:

$$\begin{aligned} f(z) &= 1 - \zeta \cos\left(\frac{\pi z}{2h_c} + \frac{\pi}{4}\right) \\ g(z) &= 1 - \psi \cos\left(\frac{\pi z}{2h_c} + \frac{\pi}{4}\right), \end{aligned} \tag{4}$$

In the above relations, ζ and ψ are the porosity and mass density coefficients, respectively, and can be expressed as [49]:

$$\zeta = 1 - \frac{E_0}{E_1}, \qquad \psi = 1 - \frac{\rho_0}{\rho_1} = 1 - \sqrt{1 - \zeta} \tag{5}$$

The porosity coefficient shows the ratio of bulk volume to the total volume. Consequently, it was found that its minimum and maximum values are zero and one, respectively. Moreover, E_0 and ρ_0 are the minimum values of Young's modulus and density, respectively.

Type B: As the second pattern of porosity distribution, symmetric cosine function is considered as follow [50]:

$$f(z) = 1 - \zeta \cos\left(\frac{\pi z}{h_c}\right), \tag{6}$$

$$g(z) = 1 - \psi \cos\left(\frac{\pi z}{h_c}\right).$$

This pattern states that the pores are distributed through the thickness of the core based on a symmetric function in which the maximum porosity occurs at the top and bottom surfaces, while the minimum porosity can be observed in the mid-plane.

Type C: Based on this type, the pore location does not depend on the z. Therefore, uniform functions with no dependence on z are employed [51]:

$$f(z) = 1 - \zeta\chi, \qquad g(z) = \sqrt{1 - \zeta\chi} \tag{7}$$

where [52]:

$$\chi = \frac{1}{\zeta} - \frac{1}{\zeta}\left(\frac{2}{\pi}\sqrt{1 - \zeta} - \frac{2}{\pi} + 1\right)^2 \tag{8}$$

On the other hand, the effect of temperature on the properties of the porous core was investigated. To this end, the following equation was used [53]:

$$P_c(T) = P_0(P_{-1} + 1 + P_1 T + P_2 T^2 + P_3 T^3) \tag{9}$$

in which P_c is the properties of the core, and T denotes the temperature in Kelvin. Also, temperature-dependent coefficients are presented by P_i ($i = -1, 0, 1, 2, 3$). Table 1 [31] lists the values of these coefficients for SUS304 which is used in the studied core.

Table 1 Coefficients of temperature-dependent properties of the porous core (SUS304) [31]

Properties	P_{-1}	P_0	P_1	P_2	P_3
$E_c\ (Pa)$	0	201.04×10^9	3.079×10^{-4}	-6.534×10^{-7}	0
$\alpha_c\ (/K)$	0	12.33×10^{-6}	8.086×10^{-4}	0	0
$\rho_c\ (kg/m^3)$	0	8166	0	0	0
ν_c	0	0.3262	-2.002×10^{-4}	3.797×10^{-7}	0

2.2.2 FG-CNTRC face sheets

The stiffness components of the FG-CNTRC faces are determined via the following relations:

$$Q_{11}^{t,b} = \frac{E_{11}}{1-\nu^2}, \qquad Q_{55}^{t,b} = G_{12} \tag{10}$$

in which t and b superscripts denote the top and bottom faces, respectively, and E_{11} and G_{12} are effective values of Young's elasticity and shear moduli of the skins, respectively. Among the different methods used to determine these effective values, the ERM as selected due to its simplicity and accuracy. The mentioned values were determined using the following equations [8]:

$$E_{11} = \eta_1 E_{11CNT} V_{CNT} + V_m E_m, \tag{11}$$

$$\frac{\eta_3}{G_{12}} = \frac{V_{CNT}}{G_{12CNT}} + \frac{V_m}{G_m} \tag{12}$$

where the subscripts CNT and m denote the CNTs reinforcement and matrix, respectively. Also, η_1 and η_3 are efficiency parameters of CNTs that can be achieved based on the molecular dynamics for different volume fractions of CNTs. It is noteworthy that the total volume of the faces (i.e. the summation of V_{CNT} and V_m) should equal one. Furthermore, other properties of the faces such as effective density and thermal expansion coefficient can also be determined by the ERM as [54]:

$$\rho^{t,b} = V_{CNT}\rho^{CNT} + V_m\rho^m, \tag{13}$$

$$\alpha_{11}^{t,b} = V_{CNT}\alpha_{11}^{CNT} + V_m\alpha_{11}^m \tag{14}$$

On the other hand, the Poisson's ratio of the faces can be expressed as:

$$v_{12} = V_{CNT}^* v_{12}^{CNT} + V_m v_m \tag{15}$$

in which, V_{CNT}^* is the CNTs' volume fraction:

$$V_{CNT}^* = \frac{w_{CNT}}{w_{CNT} + \left(\frac{\rho_{CNT}}{\rho_m}\right) - \left(\frac{\rho_{CNT}}{\rho_m}\right) w_{CNT}} \tag{16}$$

Table 2 Thermo-mechanical properties of PMMA [55]

Properties	
E_m (GPa)	$3.52–0.0034 \times T$
$\alpha_m\ (/K)$	$45 \times (1 + 0.0005 \times \Delta T) \times 10^{-6}$
$\rho_m\ (kg/m^3)$	1150
ν_m	0.34

Here, w_{CNT} is the mass fraction of CNTs. Similar to the core, the CNTs are distributed across the faces based on different patterns. These patterns determine the CNTs' placement along the thickness of the face sheets. Therefore, the following functions are suggested to consider the variations of CNTs' volume fraction [31]:

$$V_{CNT}^{t,b} = V_{CNT}^* \qquad \text{UD} \tag{17}$$

$$V_{CNT}^{t,b} = \left[1 - \frac{2}{h_{t,b}}\left(z \mp \frac{h_c + h_{t,b}}{2}\right)\right] V_{CNT}^* \qquad \text{FG - A}$$

$$V_{CNT}^{t,b} = \left[1 + \frac{2}{h_{t,b}}\left(z \mp \frac{h_c + h_{t,b}}{2}\right)\right] V_{CNT}^* \qquad \text{FG - V}$$

$$V_{CNT}^{t,b} = 2\left[1 - \frac{2}{h_{t,b}}\left(z \mp \frac{h_c + h_{t,b}}{2}\right)\right] V_{CNT}^* \qquad \text{FG - O}$$

$$V_{CNT}^{t,b} = \frac{4}{h_{t,b}}\left[\left|z \mp \frac{h_c + h_{t,b}}{2}\right|\right] V_{CNT}^* \qquad \text{FG - X}$$

where the upper sign (i.e., minus) is for to the top face, and the bottom sign (i.e., plus) represents the bottom face. It is important to note that the dispersion of CNTs in the top and bottom layers are symmetric relative to the mid-plane of structure.

The mechanical properties of the faces are also temperature dependent. Therefore, the temperature dependency of both CNTs reinforcements and matrix should be considered. To this end, the temperature-dependent properties of PMMA matrix including Young's elasticity modulus, thermal expansion coefficient, mass density, and Poisson's ratio are presented in Table 2 [55]. Note that in this table, ΔT is the temperature difference which changed linearly. Also, CNTs properties at different temperatures are presented in Table 3 [56]. Based on this table, the following polynomial can describe their dependence on the temperature [2]:

$$P_{CNT}(T) = P_0(1 + P_1\Delta T + P_2\Delta T^2 + P_3\Delta T^3) \tag{18}$$

P_0, P_1, $P_{2,}$ and P_3 are CNTs' temperature-dependent coefficients, which are shown in Table 4 [44]. Moreover, the

Table 3 Temperature-dependent properties of the facesheets' reinforcements (CNTs) [56]

T (Kelvin)	E_{11} (TPa)	G_{12} (TPa)	α_{11} ($\times 10^{-6}$ /K)
300	5.6466	1.9445	3.4584
500	5.5308	1.9643	4.5361
700	5.4744	1.9644	4.6677
1000	5.2814	1.9451	4.2800

Table 4 Coefficients of CNTs' temperature-dependent properties [44]

	P_0	P_1	P_2	P_3
E_{11}/E_{011}	1	-1.5849×10^{-4}	3.5390×10^{-7}	-3.7070×10^{-10}
G_{12}/G_{012}	1	8.3093×10^{-5}	-1.7803×10^{-7}	8.5651×10^{-11}
α_{11}/α_{011}	1	2.5039×10^{-3}	-5.3839×10^{-6}	3.2738×10^{-9}

density and Poisson's ratio of CNTs are 1400 kg/m^3 and 0.175, respectively.

2.3 Kinematic relations

To describe the displacements of the micro-curved beam, the following HSDT was chosen as the displacement field [57]:

$$u(x,z,t) = u_0(x,t) - z\frac{\partial}{\partial x}w_0(x,t) + \Phi(z)\gamma(x,t), \tag{19}$$

$$w(x,z,t) = w_0(x,t)$$

in which u and w are the displacements of each point in circumferential and radial directions, respectively. u_0 and w_0 represent the same ones but for the mid-plane. γ is the rotation of cross-section, and $\Phi(z)$ denotes the shear deformation function. Various theories have been developed to analyze the structure's displacements some of which neglect the shear deformation effects; whereas others take then into account. Here, the shear deformation effect was investigated as higher order ones leading to the more complex and also, more accurate and reliable results. The following higher order shear deformation function was considered which is also known as third-order or parabolic shear deformation theory [58]:

$$\Phi(z) = z(1 - 4z^2/3h^2) \tag{20}$$

Here, h is the total thickness of the structure, i.e., the summation of h_t, h_c, and h_b. Based on the von Karman's assumptions, the strain–displacement relations are given as follows:

$$\varepsilon_{xx} = \frac{\partial}{\partial x}u(x,z,t) + \frac{w(x,z,t)}{R},$$

$$\varepsilon_{yy} = \frac{\partial}{\partial x}v(x,z,t),$$

$$\gamma_{xy} = \frac{\partial}{\partial y}u(x,z,t) + \frac{\partial}{\partial x}v(x,z,t), \tag{21}$$

$$\gamma_{yz} = \frac{\partial}{\partial y}w(x,z,t) + \frac{\partial}{\partial z}v(x,z,t),$$

$$\gamma_{xz} = \left(\frac{\mathrm{d}}{\mathrm{d}z}\Phi(z)\right)\gamma(x,t) - \frac{u_0(x,t)}{R} + \frac{z}{R}\frac{\partial}{\partial x}w_0(x,t) - \frac{\Phi(z)\gamma(x,t)}{R}$$

Inserting the displacement components of Eq. (19) into Eq. (21), the non-zero stains can be obtained as:

$$\varepsilon_{xx} = \frac{\partial}{\partial x}u_0(x,t) - z\frac{\partial^2}{\partial x^2}w_0(x,t) + \Phi(z)\frac{\partial}{\partial x}\gamma(x,t) + \frac{w_0(x,t)}{R}, \tag{22}$$

$$\gamma_{xz} = \left(\frac{\mathrm{d}}{\mathrm{d}z}\Phi(z)\right)\gamma(x,t) - \frac{u_0(x,t)}{R} + \frac{z}{R}\frac{\partial}{\partial x}w_0(x,t) - \frac{\Phi(z)\gamma(x,t)}{R}$$

2.4 Modified couple stress theory

Since the classical elasticity theory fails to investigate the structure at small dimensions, and as the present study is aimed to consider the structure in the micro-dimension, the MCST was selected. The MCST suggests a material length-scale parameter and the strain energy of the structure which includes two parts: one related to the classical elasticity theory and the other relevant to the deviator part of the couple stress tensor as [59]:

$$U = \frac{1}{2}\int_V (\sigma : \varepsilon + \mathrm{m} : \chi)\,\mathrm{dv} \tag{23}$$

in which χ and m are the symmetric part of the curvature tensor and deviatoric part of the couple stress tensor, respectively, which can be obtained as:

$$\mathrm{m}_{ij} = 2l^2\mu(z)\chi_{ij} \tag{24}$$

where l is the material length-scale parameter of MCST, and $\mu(z)$ is the Lame's parameter.

To determine the components of the symmetric part of the curvature tensor, the following relations were employed [60]:

$$\chi_{ij} = \frac{1}{2}\left[\Theta_{i,j} + \Theta_{j,i}\right], \tag{25}$$

$$\Theta = \frac{1}{2}\nabla \times \mathrm{u} \tag{26}$$

In the above relations, Θ is the rotation vector, and u denotes displacements vector. As a result, the non-zero components of the symmetric part of the curvature tensor can be achieved:

$$\chi_{xy} = -\frac{1}{2}\frac{\partial^2}{\partial x^2}w_0(x,t) + \frac{1}{4}\left(\frac{\mathrm{d}}{\mathrm{d}z}\Phi(z)\right)\frac{\partial}{\partial x}\gamma(x,t) + \frac{1}{4R}\left(\frac{\partial}{\partial x}u_0(x,t) - z\frac{\partial^2}{\partial x^2}w_0(x,t) + \Phi(z)\frac{\partial}{\partial x}\gamma(x,t)\right), \tag{27}$$

$$\chi_{yz} = \frac{1}{4}\left(\frac{\mathrm{d}^2}{\mathrm{d}z^2}\Phi(z)\right)\gamma(x,t) + \frac{1}{4R}\left(-\frac{\partial}{\partial x}w_0(x,t) + \left(\frac{\mathrm{d}}{\mathrm{d}z}\Phi(z)\right)\gamma(x,t)\right)$$

3 Extracting the equations

3.1 Extended Hamilton's principle

Hamilton's principle and variational approach were employed to derive the governing equations. Based on the extended Hamilton's principle [61]:

$$\int_0^t \delta\left[\Pi_{ext} + K - U\right]\mathrm{d}t = 0 \tag{28}$$

in which Π_{ext}, K, and U are the external work, kinetic and strain energies, respectively. The variations of these terms should be obtained and then substituted in the above relation.

To calculate the strain energy of all three layers of the curved microbeam, the following relation can be used [62]:

$$U = \frac{1}{2}\int_x\int_y\int_{-h/2}^{h/2}\left\{\sigma^i_{xx}\varepsilon_{xx} + \sigma^i_{xz}\gamma_{xz} + 2m^i_{xy}\chi^i_{xy} + 2m^i_{yz}\chi^i_{yz}\right\}\mathrm{dV}, \qquad i = t, b, c \tag{29}$$

By separating the integrations respect to z and defining the stress resultants and using the variational approach, the following expression can be attained for strain energy variations:

$$\delta U = \int_A \left\{\begin{array}{l} \left(-\frac{\partial}{\partial x}N_{xx} + \frac{Q_x}{R} - \frac{1}{4R}\frac{\partial}{\partial x}\alpha_1\right)\delta u_0 \\ +\left(-\frac{\partial^2}{\partial x^2}M^b_{xx} + \frac{N_{xx}}{R} - \frac{1}{R}\frac{\partial}{\partial x}P_x - \frac{1}{2}\frac{\partial^2}{\partial x^2}\alpha_1 - \frac{1}{4R}\frac{\partial^2}{\partial x^2}\alpha_2 + \frac{1}{4R}\frac{\partial}{\partial x}\alpha_5\right)\delta w_0 \\ +\left(-\frac{\partial}{\partial x}M^s_{xx} + T_x - \frac{R_x}{R} - \frac{1}{4}\frac{\partial}{\partial x}\alpha_4 - \frac{1}{4R}\frac{\partial}{\partial x}\alpha_3 + \frac{1}{4}\alpha_7 + \frac{\alpha_6}{4R}\right)\delta\gamma \end{array}\right\}\mathrm{dA} \tag{30}$$

The applied stress resultants are defined as:

$$N_{xx} = Q_{110}\frac{\partial u_0}{\partial x} - Q_{111}\frac{\partial^2 w_0}{\partial x^2} + Q_{113}\frac{\partial \gamma}{\partial x} + \frac{Q_{110}w_0}{R},$$

$$M^b_{xx} = Q_{111}\frac{\partial u_0}{\partial x} - Q_{112}\frac{\partial^2 w_0}{\partial x^2} + Q_{115}\frac{\partial \gamma}{\partial x} + \frac{Q_{111}w_0}{R},$$

$$M^s_{xx} = Q_{113}\frac{\partial u_0}{\partial x} - Q_{115}\frac{\partial^2 w_0}{\partial x^2} + Q_{114}\frac{\partial \gamma}{\partial x} + \frac{Q_{113}w_0}{R},$$

$$Q_x = Q_{556}\gamma + \frac{1}{R}\left(-Q_{550}u_0 + Q_{551}\frac{\partial w_0}{\partial x} - Q_{553}\gamma\right),$$

$$P_x = Q_{557}\gamma + \frac{1}{R}\left(-Q_{551}u_0 + Q_{552}\frac{\partial w_0}{\partial x} - Q_{555}\gamma\right),$$

$$R_x = Q_{558}\gamma + \frac{1}{R}\left(-Q_{553}u_0 + Q_{555}\frac{\partial w_0}{\partial x} - Q_{554}\gamma\right),$$

$$T_x = Q_{559}\gamma + \frac{1}{R}\left(-Q_{556}u_0 + Q_{557}\frac{\partial w_0}{\partial x} - Q_{558}\gamma\right), \tag{31}$$

$$\alpha_1 = -l^2\beta_1\frac{\partial^2 w_0}{\partial x^2} + \frac{1}{2}l^2\beta_7\frac{\partial\gamma}{\partial x} + \frac{l^2}{2R}\left(\beta_1\frac{\partial u_0}{\partial x} - \beta_2\frac{\partial^2 w_0}{\partial x^2} + \beta_4\frac{\partial\gamma}{\partial x}\right),$$

$$\alpha_2 = -l^2\beta_2\frac{\partial^2 w_0}{\partial x^2} + \frac{1}{2}l^2\beta_8\frac{\partial\gamma}{\partial x} + \frac{l^2}{2R}\left(\beta_2\frac{\partial u_0}{\partial x} - \beta_3\frac{\partial^2 w_0}{\partial x^2} + \beta_6\frac{\partial\gamma}{\partial x}\right),$$

$$\alpha_3 = -l^2\beta_4\frac{\partial^2 w_0}{\partial x^2} + \frac{1}{2}l^2\beta_9\frac{\partial\gamma}{\partial x} + \frac{l^2}{2R}\left(\beta_4\frac{\partial u_0}{\partial x} - \beta_6\frac{\partial^2 w_0}{\partial x^2} + \beta_5\frac{\partial\gamma}{\partial x}\right),$$

$$\alpha_4 = -l^2\beta_7\frac{\partial^2 w_0}{\partial x^2} + \frac{1}{2}l^2\beta_{10}\frac{\partial\gamma}{\partial x} + \frac{l^2}{2R}\left(\beta_7\frac{\partial u_0}{\partial x} - \beta_8\frac{\partial^2 w_0}{\partial x^2} + \beta_9\frac{\partial\gamma}{\partial x}\right),$$

$$\alpha_5 = \frac{1}{2}l^2\beta_{11}\gamma - \frac{l^2\beta_1}{2R}\frac{\partial w_0}{\partial x} + \frac{l^2\beta_7\gamma}{2R},$$

$$\alpha_6 = \frac{1}{2}l^2\beta_{12}\gamma - \frac{l^2\beta_7}{2R}\frac{\partial w_0}{\partial x} + \frac{l^2\beta_{10}\gamma}{2R},$$

$$\alpha_7 = \frac{1}{2}l^2\beta_{13}\gamma - \frac{l^2\beta_{11}}{2R}\frac{\partial w_0}{\partial x} + \frac{l^2\beta_{12}\gamma}{2R}$$

Also, the kinetic energy of the microstructure can be calculated by [63]:

$$K = \frac{1}{2}\int_x\int_y\int_{-h/2}^{h/2}\rho(z)\left(\left(\frac{\partial u}{\partial t}\right)^2 + \left(\frac{\partial w}{\partial t}\right)^2\right)\mathrm{dV} \tag{32}$$

Replacing the displacements of Eq. (19) in the above relation, and similar to strain energy, i.e., separating the integrals respect to z and using the variational formulation, the below equation can be reached:

$$\delta K = \int_A \left\{ \begin{array}{l} \left(-I_0 \frac{\partial^2}{\partial t^2} u_0 + I_1 \frac{\partial^2}{\partial x \partial t^2} w_0 - I_3 \frac{\partial^2}{\partial t^2} \gamma \right) \delta u_0 \\ + \left(I_2 \frac{\partial^4}{\partial x^2 \partial t^2} w_0 - I_1 \frac{\partial^3}{\partial x \partial t^2} u_0 - I_5 \frac{\partial^3}{\partial x \partial t^2} \gamma - I_0 \frac{\partial^2}{\partial t^2} w_0 \right) \delta w_0 \\ + \left(-I_4 \frac{\partial^2}{\partial t^2} \gamma + I_5 \frac{\partial^3}{\partial x \partial t^2} w_0 - I_3 \frac{\partial^2}{\partial t^2} u_0 \right) \delta \gamma \end{array} \right\} \mathrm{dA} \tag{33}$$

in which:

$$\{ I_0, I_1, I_2, I_3, I_4, I_5 \} = \int_z \rho(z) \{ 1, z, z^2, \Phi(z), \Phi^2(z), z\Phi(z) \} \, \mathrm{dz} \tag{34}$$

The external work in this study consists of three parts: the first one is due to the viscoelastic substrate, the second is the result of the thermal load, while the third one is related to the applied magnetic load:

$$\Pi_{ext} = \Pi_{substrate} + \Pi_{thermo-mechanical\ load} + \Pi_{magnetic\ load} \tag{35}$$

To determine the work of the viscoelastic substrate, the visco-Pasternak type substrate was selected, which consisted of springs, shear layer, and dashpots. Therefore, the substrate force can be obtained via the following relation [64]:

$$F_{substrate} = K_1 w_0(x,t) - K_2 \nabla^2 w_0(x,t) + D \frac{\partial}{\partial t} w_0(x,t) \tag{36}$$

where K_1, K_2, and D are the springs, shear layer, and dashpots parameters, respectively.

Consequently, to obtain the work caused by the elastic substrate, the following relation may be used:

$$\delta \Pi_{substrate} = \int_x \left[-F_{substrate} \, \delta w_0(x,t) \right] \, \mathrm{dx} \tag{37}$$

Moreover, the work of thermal load can be determined using the below equation [65]:

$$\delta \Pi_{thermo-mechanical\ load} = \int_x \left[N \left(\frac{\partial w_0(x,t)}{\partial x} \right) \delta w_0(x,t) \right] \mathrm{dx} \tag{38}$$

where N includes both thermal (N_T) and mechanical (N_0) loads [66]:

$$N = N_0 + N^T, \tag{39}$$

$$N^T = \int_{-h/2}^{h/2} Q_{11}^{cf} \alpha_{11}^{cf} \Delta T \, \mathrm{dz} \tag{40}$$

The structure is exposed to longitudinal magnetic load (H_x), its force regarding Maxwell's relations can be obtained by the following equation [67]:

$$F_{magnetic\ load} = \eta H_x^2 \left(\frac{\partial^2 w}{\partial x^2} + \frac{\partial^2 w}{\partial z^2} \right) \tag{41}$$

In the above relation, magnetic field permeability is shown by η. Inserting displacements of Eq. (19) in Eq. (41) yields:

$$F_{magnetic\ load} = \eta H_x^2 \frac{\partial^2}{\partial x^2} w_0(x,t) \tag{42}$$

Therefore, the work of Lorentz force can be demonstrated by:

$$\delta \Pi_{magnetic\ load} = \int_{-h/2}^{h/2} F_{magnetic\ load} \, \delta w_0(x,t) \, \mathrm{dx\,dy} \tag{43}$$

3.2 Governing equations

Using the obtained expressions for variations of strain and kinetic energies and works of external loads and substituting them into the extended Hamilton's principle and separating coefficient of each variable, the below governing equations can be achieved in terms of displacements:

δu_0 :

$$\begin{aligned} & -Q_{110} \frac{\partial^2 u_0}{\partial x^2} + Q_{111} \frac{\partial^3 w_0}{\partial x^3} \\ & \quad - Q_{113} \frac{\partial^2 \gamma}{\partial x^2} - \frac{Q_{110}}{R} \frac{\partial w_0}{\partial x} - \frac{Q_{556} \gamma}{R} + \frac{Q_{550} u_0}{R^2} - \frac{Q_{551}}{R^2} \frac{\partial w_0}{\partial x} + \frac{Q_{553} \gamma}{R^2} \\ & \quad + \frac{l^2 \beta_1}{4R} \frac{\partial^3 w_0}{\partial x^3} - \frac{l^2 \beta_7}{8R} \frac{\partial^2 \gamma}{\partial x^2} - \frac{l^2 \beta_1}{8R^2} \frac{\partial^2 u_0}{\partial x^2} + \frac{l^2 \beta_2}{8R^2} \frac{\partial^3 w_0}{\partial x^3} - \frac{l^2 \beta_4}{8R^2} \frac{\partial^2 \gamma}{\partial x^2} \\ & \quad + I_0 \frac{\partial^2 u_0}{\partial t^2} - I_1 \frac{\partial^3 w_0}{\partial x \partial t^2} + I_3 \frac{\partial^2 \gamma}{\partial t^2} = 0 \end{aligned} \tag{44}$$

δw_0 :

$$\begin{aligned} & \frac{Q_{110}}{R} \frac{\partial u_0}{\partial x} + \frac{Q_{113}}{R} \frac{\partial \gamma}{\partial x} + \frac{Q_{110} w_0}{R^2} - \frac{Q_{557}}{R} \frac{\partial \gamma}{\partial x} \\ & \quad + \frac{Q_{551}}{R^2} \frac{\partial u_0}{\partial x} - \frac{Q_{552}}{R^2} \frac{\partial^2 w_0}{\partial x^2} + \frac{Q_{555}}{R^2} \frac{\partial \gamma}{\partial x} + \eta H_x^2 \frac{\partial^2 w_0}{\partial x^2} \\ & \quad - 2 \frac{Q_{111}}{R} \frac{\partial^2 w_0}{\partial x^2} + \frac{1}{2} l^2 \beta_1 \frac{\partial^4 w_0}{\partial x^4} - \frac{1}{4} l^2 \beta_7 \frac{\partial^3 \gamma}{\partial x^3} \\ & \quad - \frac{l^2 \beta_8}{8R} \frac{\partial^3 \gamma}{\partial x^3} - \frac{l^2 \beta_2}{8R^2} \frac{\partial^3 u_0}{\partial x^3} + \frac{l^2 \beta_3}{8R^2} \frac{\partial^4 w_0}{\partial x^4} \\ & \quad - \frac{l^2 \beta_6}{8R^2} \frac{\partial^3 \gamma}{\partial x^3} + \frac{l^2 \beta_{11}}{8R} \frac{\partial \gamma}{\partial x} - \frac{l^2 \beta_1}{8R^2} \frac{\partial^2 w_0}{\partial x^2} \\ & \quad + \frac{l^2 \beta_7}{8R^2} \frac{\partial \gamma}{\partial x} - \frac{l^2 \beta_1}{4R} \frac{\partial^3 u_0}{\partial x^3} + \frac{l^2 \beta_2}{2R} \frac{\partial^4 w_0}{\partial x^4} - \frac{l^2 \beta_4}{4R} \frac{\partial^3 \gamma}{\partial x^3} \\ & \quad - Q_{111} \frac{\partial^3 u_0}{\partial x^3} + Q_{112} \frac{\partial^4 w_0}{\partial x^4} - Q_{115} \frac{\partial^3 \gamma}{\partial x^3} + I_0 \frac{\partial^2 w_0}{\partial t^2} \\ & \quad + I_1 \frac{\partial^3 u_0}{\partial x \partial t^2} - I_2 \frac{\partial^4 w_0}{\partial x^2 \partial t^2} + I_5 \frac{\partial^3 \gamma}{\partial x \partial t^2} \\ & \quad + N^T \frac{\partial^2 w_0}{\partial x^2} - K_2 \frac{\partial^2 w_0}{\partial x^2} - D \frac{\partial w_0}{\partial t} + K_1 w_0 + N_0 \frac{\partial^2 w_0}{\partial x^2} = 0 \end{aligned} \tag{45}$$

$\delta\gamma$:

$$
\begin{aligned}
&\frac{1}{8}l^2\beta_{13}\gamma-\frac{l^2\beta_{11}}{8R}\frac{\partial w_0}{\partial x}+\frac{l^2\beta_7}{8R^2}\frac{\partial w_0}{\partial x}-\frac{l^2\beta_{10}\gamma}{8R^2}\\
&-\frac{l^2\beta_7}{8R}\frac{\partial^2 u_0}{\partial x^2}+\frac{l^2\beta_8}{8R}\frac{\partial^3 w_0}{\partial x^3}-\frac{l^2\beta_9}{4R}\frac{\partial^2\gamma}{\partial x^2}+\frac{l^2\beta_4}{4R}\frac{\partial^3 w_0}{\partial x^3}\\
&-\frac{l^2\beta_4}{8R^2}\frac{\partial^2 u_0}{\partial x^2}\\
&+\frac{l^2\beta_6}{8R^2}\frac{\partial^3 w_0}{\partial x^3}-\frac{l^2\beta_5}{8R^2}\frac{\partial^2\gamma}{\partial x^2}-Q_{113}\frac{\partial^2 u_0}{\partial x^2}+Q_{115}\frac{\partial^3 w_0}{\partial x^3}-Q_{114}\frac{\partial^2\gamma}{\partial x^2}+I_3\frac{\partial^2 u_0}{\partial t^2}\\
&-I_5\frac{\partial^3 w_0}{\partial x\partial t^2}+I_4\frac{\partial^2\gamma}{\partial t^2}+\frac{Q_{553}u_0}{R^2}\\
&-\frac{Q_{555}}{R^2}\frac{\partial w_0}{\partial x}+\frac{Q_{554}\gamma}{R^2}-\frac{Q_{113}}{R}\frac{\partial w_0}{\partial x}+Q_{559}\gamma-\frac{1}{8}l^2\beta_{10}\frac{\partial^2\gamma}{\partial x^2}\\
&+\frac{1}{4}l^2\beta_7\frac{\partial^3 w_0}{\partial x^3}-\frac{Q_{556}u_0}{R}-2\frac{Q_{558}\gamma}{R}+\frac{Q_{557}}{R}\frac{\partial w_0}{\partial x}=0
\end{aligned}
\tag{46}
$$

in which:

$$
Q_{iij}=\int_{-h/2}^{h/2} Q_{ii}\,z^j\,\mathrm{d}z,\qquad i=1,5;\qquad j=0,1,2 \tag{47}
$$

$$
\left\{Q_{ii3},\ Q_{ii4},\ Q_{ii5}\right\}=\int_{-h/2}^{h/2} Q_{ii}\left\{\Phi(z),\ \Phi^2(z),\ z\Phi(z)\right\}\mathrm{d}z,\qquad i=1,5
$$

$$
\left\{Q_{556},\ Q_{557},\ Q_{558},\ Q_{559}\right\}
=\int_{-h/2}^{h/2} Q_{55}\left\{\frac{\mathrm{d}}{\mathrm{d}z}\Phi(z),\ z\left(\frac{\mathrm{d}}{\mathrm{d}z}\Phi(z)\right),\ \Phi(z)\left(\frac{\mathrm{d}}{\mathrm{d}z}\Phi(z)\right),\ \left(\frac{\mathrm{d}}{\mathrm{d}z}\Phi(z)\right)^2\right\}\mathrm{d}z,
$$

$$
\beta_k=\int_{-h/2}^{h/2}\mu(z)\,z^{k-1}\,\mathrm{d}z,\qquad k=1,2,3
$$

$$
\left\{\beta_4,\ \beta_5,\ \beta_6,\ \beta_7\right\}=\int_{-h/2}^{h/2}\mu(z)\left\{\Phi(z),\ \Phi^2(z),\ z\Phi(z),\ \frac{\mathrm{d}}{\mathrm{d}z}\Phi(z)\right\}\mathrm{d}z,
$$

$$
\left\{\beta_8,\ \beta_9,\ \beta_{10}\right\}=\int_{-h/2}^{h/2}\mu(z)\left\{z\left(\frac{\mathrm{d}}{\mathrm{d}z}\Phi(z)\right),\ \Phi(z)\left(\frac{\mathrm{d}}{\mathrm{d}z}\Phi(z)\right),\ \left(\frac{\mathrm{d}}{\mathrm{d}z}\Phi(z)\right)^2\right\}\mathrm{d}z,
$$

$$
\left\{\beta_{11},\ \beta_{12},\ \beta_{13}\right\}=\int_{-h/2}^{h/2}\mu(z)\left\{\frac{\mathrm{d}^2}{\mathrm{d}z^2}\Phi(z),\ \left(\frac{\mathrm{d}^2}{\mathrm{d}z^2}\Phi(z)\right)\left(\frac{\mathrm{d}}{\mathrm{d}z}\Phi(z)\right),\ \left(\frac{\mathrm{d}^2}{\mathrm{d}z^2}\Phi(z)\right)^2\right\}\mathrm{d}z
$$

4 Analytical solution

To solve the governing equations and extracting the results, the analytical Navier's solution method was employed for both ends of a simply supported curved microbeam. To satisfy the geometrical boundary condition, the following functions are introduced for the displacements [68]:

$$
\begin{Bmatrix} u_0\\ w_0\\ \gamma\end{Bmatrix}=\sum_{m=1}^{\infty}\begin{Bmatrix} U_m\ \cos(\Xi x)\\ W_m\ \sin(\Xi x)\\ \Upsilon_m\ \cos(\Xi x)\end{Bmatrix}\mathrm{e}^{\mathrm{i}\omega t} \tag{48}
$$

in which U, W, and Υ are the unknowns, and m represents the number of the axial wave. Also, Ξ is defined as $m\pi/L$.

Substituting the defined functions of Eq. (48) in the governing equations of (44)–(46) leads to the following matrix form for the vibrational and buckling analyses:

4.1 Vibration analysis

Solving the eigenvalue problem of Eq. (49) in the following form leads to the natural frequencies of the micro-curved beam:

$$
\left([K]+\mathrm{i}\omega[C]-\omega^2[M]\right)\{X\}=0 \tag{49}
$$

In the above relation, $[K]$, $[C]$, and $[M]$ are the stiffness, damping, and mass matrices, and $\{X\}$ is displacements vector which includes $\{U,\ W,\ \Upsilon\}^T$. ω denotes the natural frequency.

4.2 Buckling analysis

By dropping down the mass and damping matrices and setting the $N_0=-P_{cr}$, the following eigenvalue equation can be used to determine the critical buckling load:

$$
\left([K]-P_{cr}\left[K_g\right]\right)\{X\}=0 \tag{50}
$$

where $[K_g]$ is the geometric stiffness matrix.

The components of stiffness, damping, and mass matrices are presented in the "Appendix".

5 Results and discussion

In the previous sections, the governing equations of a three-layered micro-curved beam exposed to a longitudinal magnetic load rested on the viscoelastic substrate were derived. Navier's solution method was employed to solve these equations for simply supported edges. In this section, the numerical results are presented in two different parts, namely, vibrational and buckling responses, and the effect of various parameters on them was discussed.

5.1 Vibration analysis results

To obtain the natural frequencies of the microstructure, the eigenvalue problem of Eq. (49) should be solved. First, the reliability of the results was examined through a comparison of a simpler state with the previously published reports. To this goal, and due to the absence of similar work to compare with, some parameters have neglected the results were obtained for simpler cases. In this regard, the faces were ignored and the curvature radius was tended to infinity which implies a straight beam. The results for a microbeam were extracted and compared to those of Ansari et al. [69], and Ma et al. [70] as listed in Table 5. The results of this table are extracted with $L/h = 10$, $\nu = 0.38$, $\rho = 1220$ kg/m^3, $E = 1.44$ *GPa* and $l = 17.6$ µm. The current study indicated an excellent consistency with the previous results reflecting the reliability of our framework. As the second step to ensure the validity of the results, they were compared with those of Ansari et al. [69], Zhang et al. [71], and Allahkarami et al. [72] in Table 6 which are for a single-layer homogenous curved microbeam. The results are listed for both ceramic

Table 7 Size effect on the fundamental natural frequency (*kHz*) of the curved microbeam for different types of porosity distribution

	h/l				
	1	2	4	6	8
Type A	2093.4819	716.6969	302.5902	194.0247	143.4393
Type B	2113.0777	730.5290	310.5204	199.4757	147.5738
Type C	2079.4475	712.5379	301.1939	193.2023	142.8528

Table 5 Comparing the natural frequencies (*MHz*) for single-layer micro straight beam with those of previously published works (numbers in parenthesis are percentage error)

Mode no.	$h/l = 10$			$h/l = 5$		
	Present	Ansari et al. [69]	Ma et al. [70]	Present	Ansari et al. [69]	Ma et al. [70]
1	0.0364	0.0376 (3.30)	0.03780 (3.85)	0.0751	0.0778 (3.60)	0.0778 (3.62)
2	0.1388	0.1397 (0.65)	0.1416 (2.02)	0.2758	0.2888 (4.71)	0.2887 (4.68)

Table 6 Dimensionless frequency of homogenous curved microbeam (numbers in parenthesis are percentage error)

Material type	Source			
	Ansari et al. [69]	Zhang et al. [71]	Allahkarami et al. [72]	Present
Ceramic	0.8538 (– 0.15)	0.8557 (0.07)	0.8544 (– 0.08)	0.8551
Metal	0.3863 (1.34)	0.3808 (– 0.10)	0.3822 (0.26)	0.3812

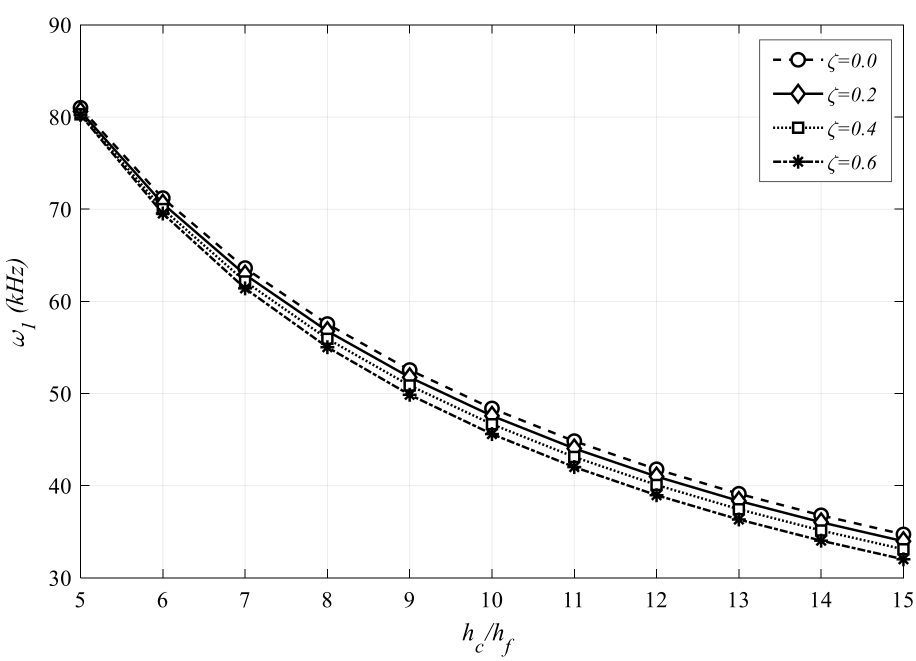

Fig. 4 Effect of porosity and thicknesses ratio variations on the fundamental natural frequency of the micro structure

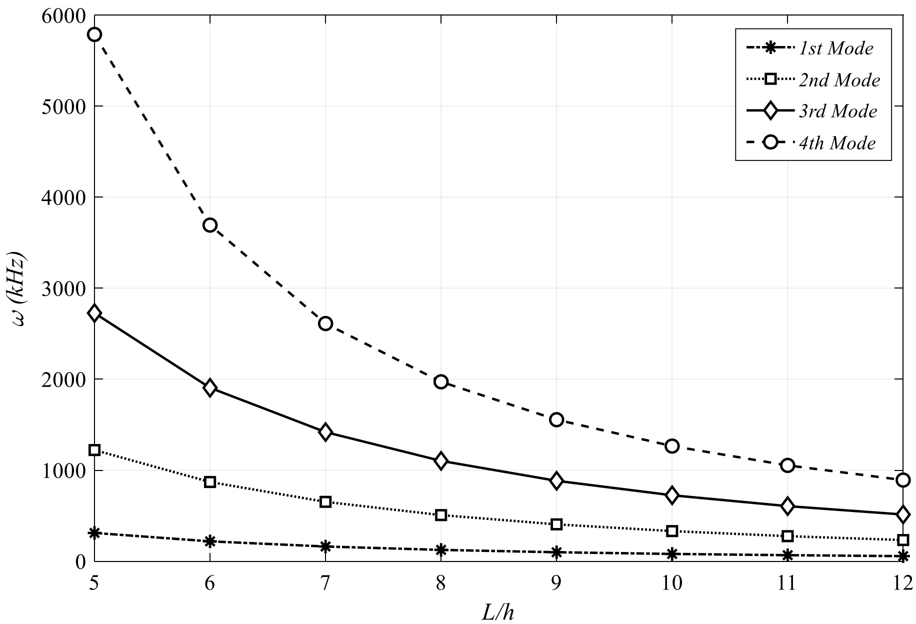

Fig. 5 Slenderness ratio variations effects on the first four natural frequencies

(i.e. SiC) and metal (i.e. aluminum) structure with the following mechanical properties: $E_m = 70\ GPa$, $\rho_m = 2702$ kg/m^3, $\nu_m = 0.3$, $E_c = 427\ GPa$, $\rho_c = 3100$ kg/m^3, and $\nu_c = 0.17$. Also, the results were obtained for the length-scale parameter of 15 μm and the central opening angle of $\pi/4$ with $h/l = 2$, and $L/h = 20$. It should be noted that the dimensionless natural frequency in Table 6 is defined as $\Omega = \omega L\sqrt{I_0/Q_{110}}$. This research showed an excellent agreement with the previously published works. Therefore, again the reliability of the equations, solution method, and finally the results is confirmed.

In the following, the effects of different parameters on the natural frequencies of the considered structure (i.e., the three-layered curved microbeam) will be investigated. It should be noted that the efficiency parameters of CNTs were introduced in Eqs. (11)–(12) for $V_{CNT} = 0.11$ as $\eta_1 = 0.143$ and $\eta_3 = 0.934$; for $V_{CNT} = 0.14$, as $\eta_1 = 0.150$ and $\eta_3 = 0.941$, and for $V_{CNT} = 0.17$ as $\eta_1 = 0.149$ and $\eta_3 = 1.381$ [73]. For all the presented results except those mentioned, the following specifications were used: $h_c/l = 10$, $h_t = h_b$, the core thickness was five times higher than that of the faces, $L = 10\ h$, and $\theta = \pi/2$. Moreover, the relationship between the central opening angle and length was $L = R\theta$.

Figure 4 considers the effect of the porosity coefficient and also thicknesses ratio on the first natural frequency. As

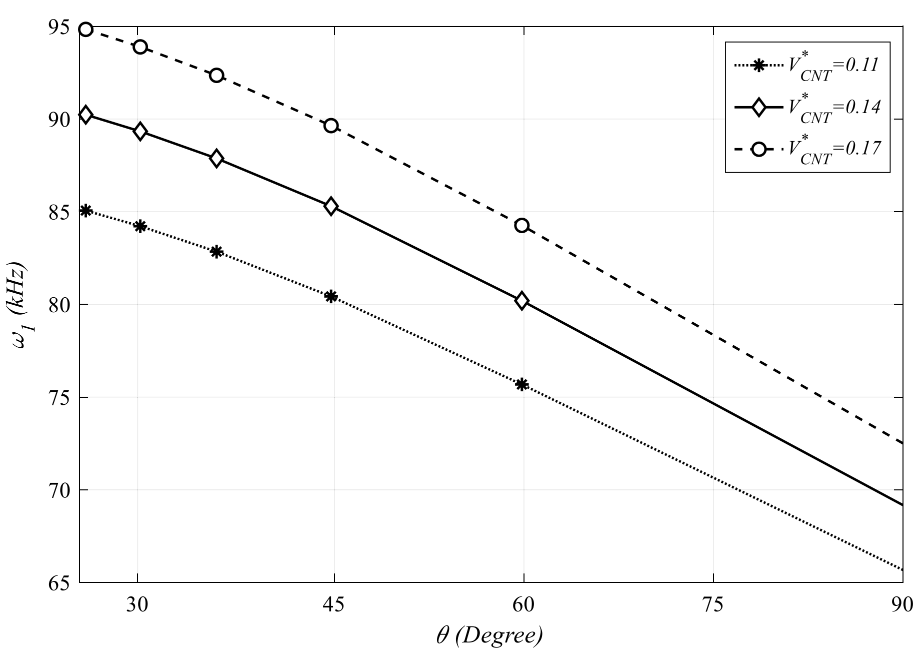

Fig. 6 Central opening angle and CNTs' volume fractions variations effect on the natural frequency

mentioned before, the porosity coefficient refers to the void to bulk volume and its enhancement from zero means the increment of the pore volume. Therefore, it is expected that both stiffness and density of the structure reduce. On the other hand, it is well known that the frequency is generally proportional to the square root of stiffness-to-mass ratio. Thus, an increase in the porosity coefficient declines the mass more than stiffness, accordingly, the frequency will decrease. A rise in the h_c/h_f ratio decremented the natural frequency. Since the stiffness of the faces is much higher than the core, for constant total thickness, an increase in the core thickness means a reduction in the thickness of the faces, therefore, the stiffness of the structure will reduce giving rise to a reduction in the natural frequencies.

Table 7 lists the exact values of natural frequencies for different dimensionless length-scale parameter (*h*/*l*) and porosity distribution types. As the *h*/*l* ratio grew, the frequencies decreased due to a reduction in stiffness. The results for different patterns of porosity distribution suggest that type C which (a uniform pores distribution) exhibited the least results, while type B (the symmetric pattern) caused the maximum values. In type B, the most stiffness occurred on the core surfaces causing higher stiffness compared to two other types.

Fig. 7 Influence of temperature changes on the frequencies for different values of central opening angle

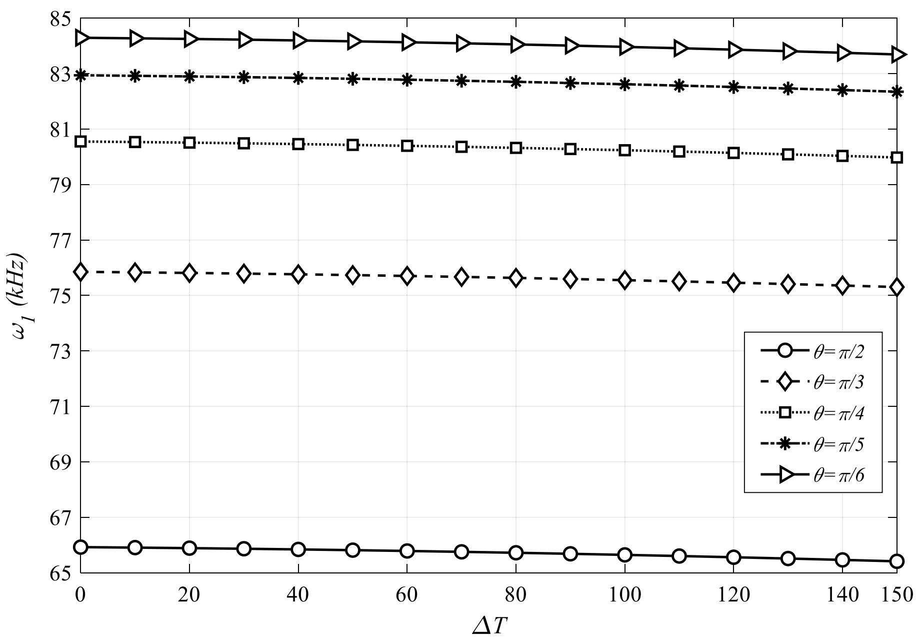

Fig. 8 Magnetic field effect on the frequencies for various types of CNTs' dispersion

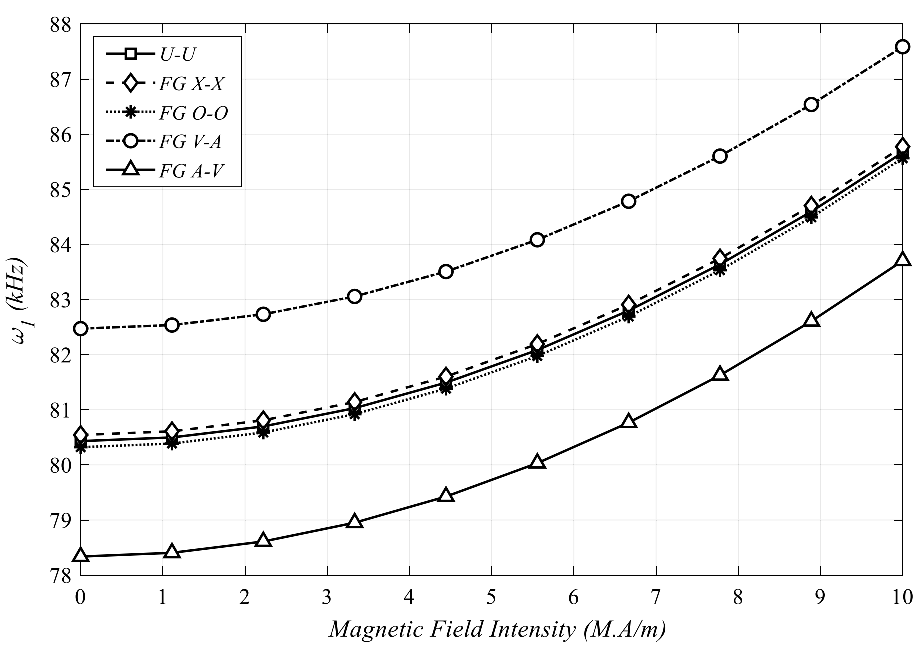

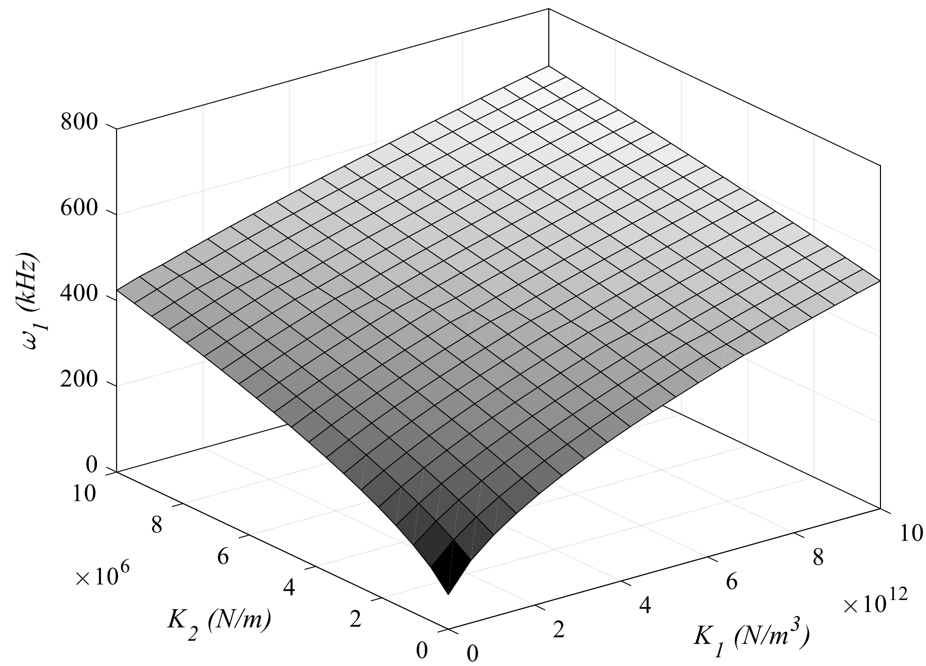

Fig. 9 Springs and shear layer parameters' variations effect on the fundamental natural frequency

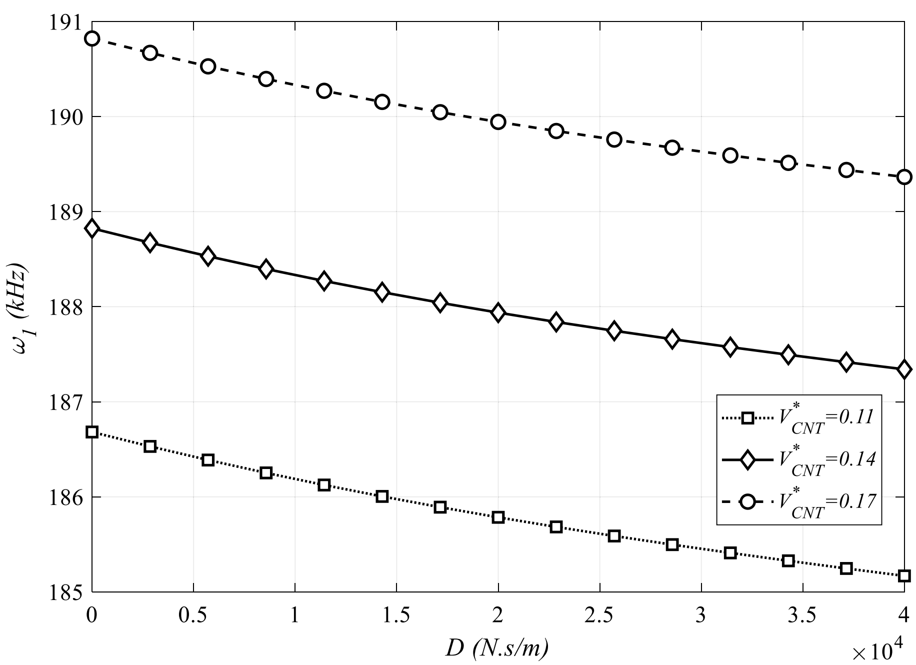

Fig. 10 Dashpots' parameter variations effect on the first natural frequency

The effect of the beam slenderness on the natural frequencies of the first four modes is illustrated in Fig. 5. By enhancing the length of the curved microbeam relative to its thickness, the natural frequencies reduced due to a decline in the structure stiffness. This phenomenon occurs for all first four modes. Note that the number of modes is specified by *m*.

Figure 6 shows the effects of CNTs volume fraction and the central opening angle (in Radian) on the fundamental natural frequency of the microstructure. By raising the content of CNTs in the faces, the faces, and thus the structure, got stiffer due to their extreme stiffness. The natural frequencies enhanced by increasing the volume fraction of CNTs. Furthermore, incrementing the central opening angle (i.e. length to curvature radius ratio) decremented the frequency. In other words, at a constant length, increasing θ elongated the beam, and similar to the previous findings, the natural frequencies showed a decline.

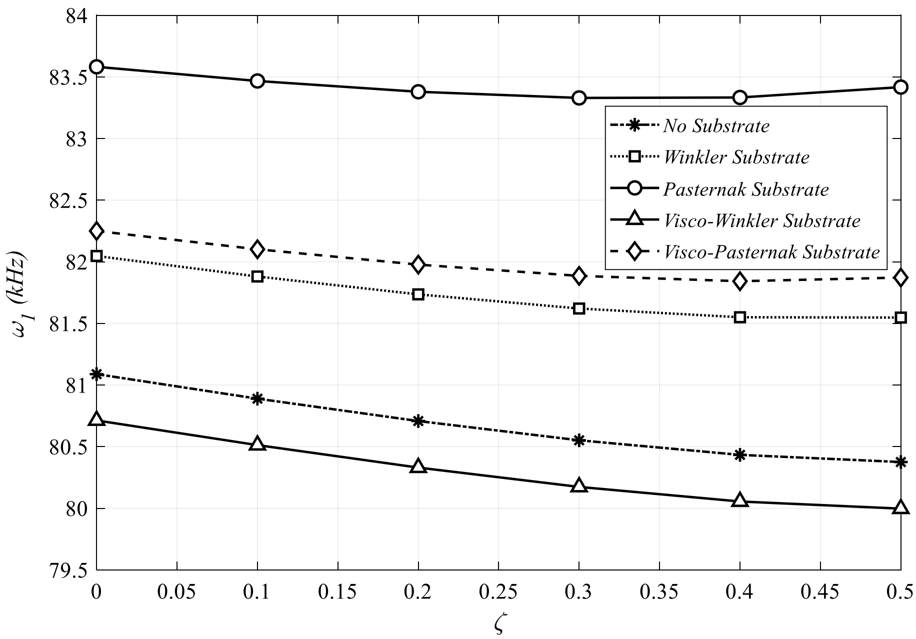

Fig. 11 Comparing different types of substrate and their effect on the frequency of the micro structure

Table 8 Comparing the dimensionless critical buckling load for single-layer macro straight beam with those of previously published works ($P^*_{cr} = P_{cr}L^2/EI$) (numbers in parenthesis are percentage error)

$L/h = 100$				$L/h = 20$			
Present	Reddy [74]	Aydogdu [75]	Eltaher et al. [76]	Present	Reddy [74]	Aydogdu [75]	Eltaher et al. [76]
9.8598	9.8671 (0.07)	–	–	9.8475	9.8696 (0.22)	9.8696 (0.22)	9.86973 (0.23)

The influence of temperature variations is examined in Fig. 7 for the different central opening angles. As can be seen in this figure, an increase in the temperature caused a slight reduction in the natural frequencies due to a drop in the stiffness of the microstructure. Also, comparing the curves for the different central opening angles confirmed the previous findings on its effect expressing that an increase in θ will decrease the natural frequency.

A longitudinal magnetic load was applied to the structure whose effect is investigated in Fig. 8. An increase in the magnetic field intensity made the structure stiffer, hence, the frequencies showed an increment. Moreover, Fig. 8 compares the effect of different patterns of CNTs dispersion on the natural frequencies. It was found that the FG-VA pattern resulted in the maximum values, while FG-AV led to the lowest ones. Since in the FG-VA pattern, the CNTs are more abundant in the surfaces of the structure, its stiffness is more than other patterns. In the FG-AV pattern, fewer CNTs can be found on surfaces which explains why the frequencies are the lowest in this pattern.

The effect of the parameters of the substrate on the natural frequencies of the microstructure is illustrated in Figs. 9, 10, 11. Figure 9 considers K_1 and K_2 influences (related to the springs and shear layer, respectively). An increment in both these parameters enhanced the natural frequencies due to the rigidity augmentation. Figure 10 considers the effect of the dashpots parameter, i.e., D. Unlike two other substrate's parameters, a rise in the dashpots decremented the natural frequencies which occurred for all studied volume fractions of CNTs. Furthermore, a comparison between different types of substrates is made in Fig. 11. While the visco-Winkler type of substrate led to lower frequencies in comparison to the substrate-free case, the addition of the substrate to the structure enhanced its rigidity and accordingly, its frequencies. Based on this figure, the Pasternak type of substrate, which includes springs and shear layer, led to the highest frequencies.

5.2 Buckling analysis results

Here, the results for the mechanical buckling response are presented. Similar to the vibration results, first, the results were compared with previous reports. To this end, the eigenvalue problem of Eq. (50) was solved, and the dimensionless critical buckling load of a macro straight beam was determined by setting the material length-scale parameter to zero and tending the curvature radius to infinity. The results were compared to those of Reddy [74], Aydogdu [75], and Eltaher

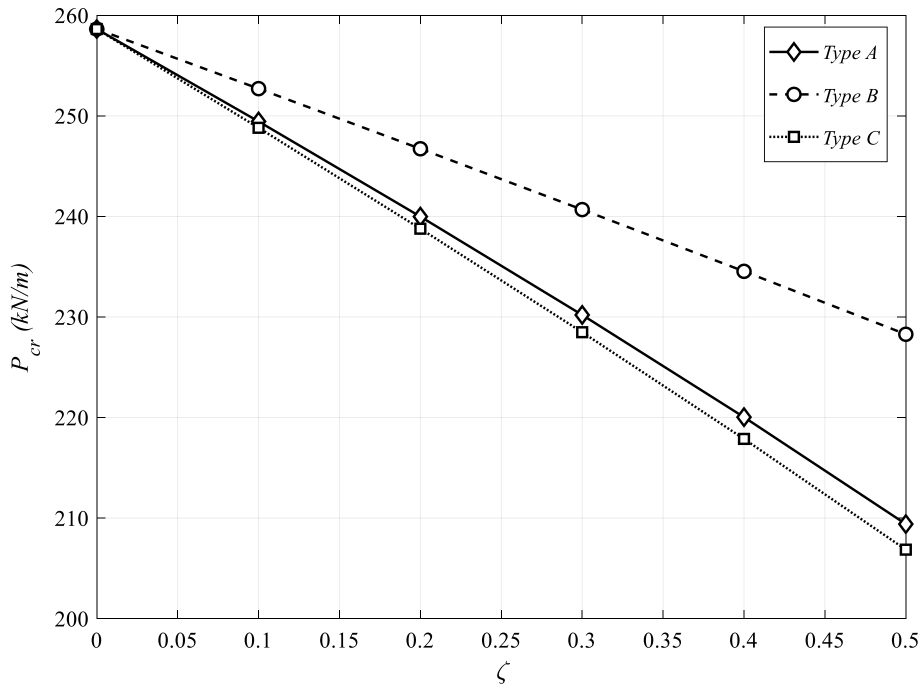

Fig. 12 Investigation the effect of porosity increasing for three types of pores' distribution on the critical buckling load

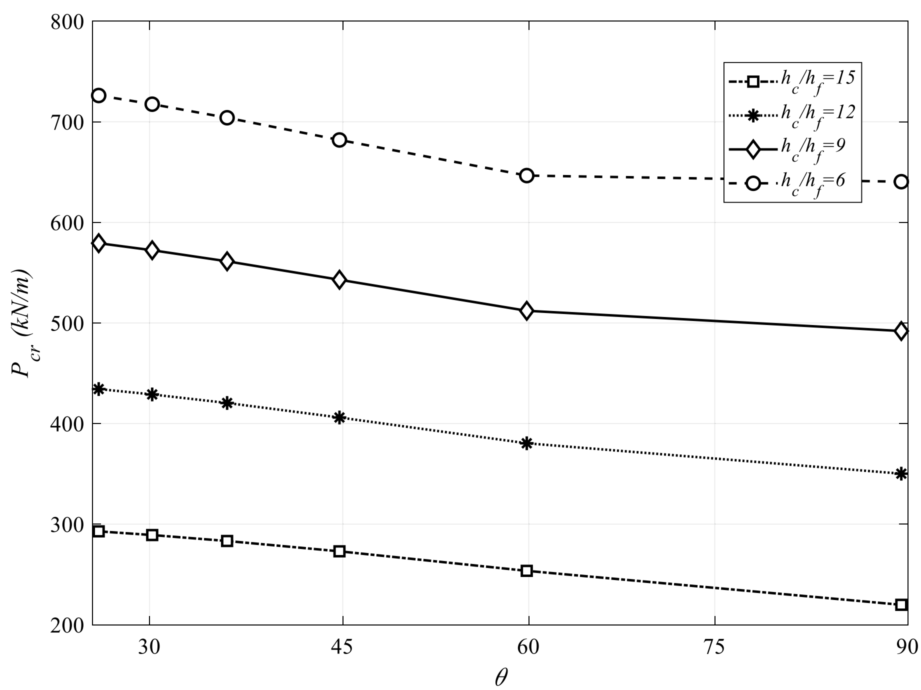

Fig. 13 Central opening angle effect on the critical buckling load for different values of thicknesses ratio

et al. [76]. The presented results in Table 8 were gained with the following properties: $L = 10$ m, $\nu = 0.3$, $\rho = 1$ kg/m^3, $E = 30$ MPa. Also, they obey the following relation to be non-dimensionalized: $P_{cr}{}^{*} = P_{cr}L^2/EI$. A good agreement can be observed between the results of the current study and the previous ones reflecting the reliability of our method. The critical buckling loads were determined for the under consideration three-layered curved microbeam with the previously mentioned specifications.

Figure 12 shows the effect of the porosity coefficient on the critical buckling load for different types of porosity distributions. The critical buckling load of the structure showed a decline by increasing the porosity due to a decline in the stiffness. Among three types of porosity distribution patterns, type C (uniform distribution) showed the least results, while type B (symmetric pattern) exhibited the highest critical buckling load.

Table 9 Various patterns of CNTs' dispersion and slenderness ratio effects on the critical buckling load (*kN/m*) of the curved microbeam

		L/h	
3	6	9	12
UU pattern			
2088.3094	613.2460	282.4105	161.4040
FG-VA pattern			
2192.3512	644.6546	296.9358	169.6939
FG-XX pattern			
2095.9054	615.0530	283.2004	161.8459
FG-OO pattern			
2080.7485	611.4509	281.6269	160.9664
FG-AV pattern			
1983.4716	581.7797	267.8771	153.1138

Figure 13 depicts the simultaneous effects of the central opening angle and thicknesses ratio. An increase in the central opening angle caused a reduction in stiffness by increasing the length, hence, the natural frequency decreased. As mentioned before, since the stiffness of the faces was more than the core, an increment in the h_c/h_f ratio declined the results. In this case, the total thickness of the structure remained constant.

Table 9 addresses the effect of slenderness ratio and CNTs dispersion patterns on the critical buckling load of the under consideration microstructure. The critical buckling load reduced as the length of the beam exceeded its thickness. Moreover, among different types of CNTs' dispersion patterns, similar to vibrational response, FG-VA and FG-AV resulted in the most and the least critical buckling loads, respectively.

Figure 14 illustrates the influences of the temperature and magnetic field intensity on the critical buckling load. The critical buckling load was reduced by increasing the temperature difference from the ambient temperature. Moreover, a rise in the intensity of the magnetic field enhanced the critical buckling load.

The effect of the parameter of the springs of the substrate is examined in Fig. 15. As can be seen, enhancement of the parameter of springs (i.e. making the structure more rigid) augmented the critical buckling load. This figure also confirms the previous results about the effect of CNTs' dispersion pattern on the critical buckling load.

Figure 16 presents the effects of two factors: volume fraction of CNTs and the shear layer parameter of the substrate. Increasing the CNTs content of the faces increased their stiffness, causing an enhancement in the critical buckling load of the microstructure. Moreover, similar to the spring parameter, enhancing the shear layer elevated the critical buckling load.

Figure 17 compares different types of substrate in terms of the length-scale to thickness variations. Based on this figure, as the *l/h* ratio increased, its critical buckling load was enhanced since the stiffness of the structure was increased. Also, regardless of its type, the inclusion of a substrate increased the critical buckling among the two considered substrates, the Pasternak foundation led to a higher critical buckling load compared to the Winkler type.

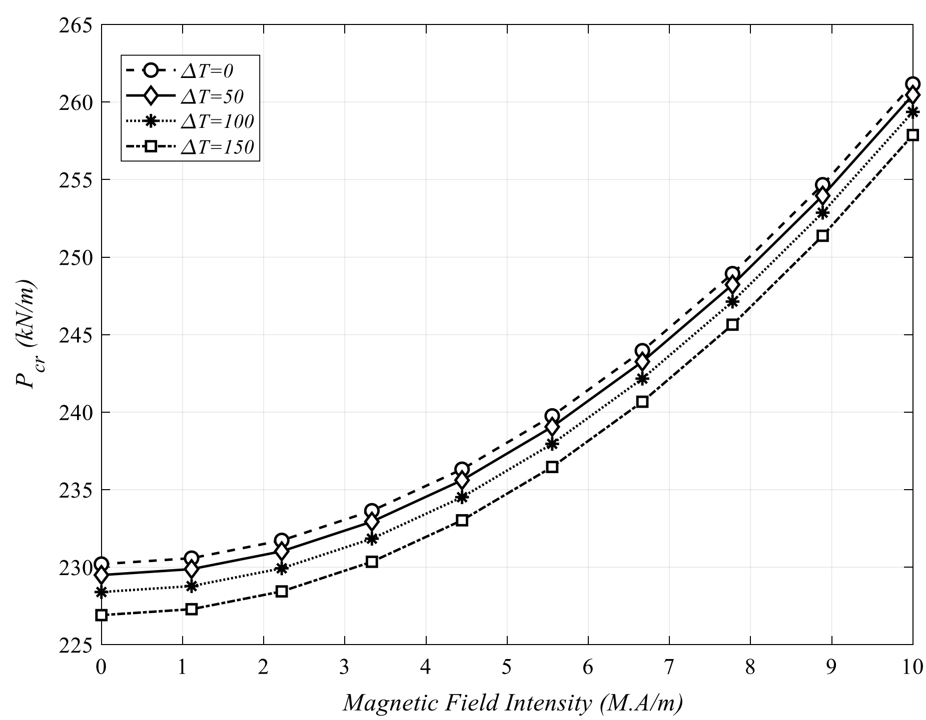

Fig. 14 Magnetic field intensity effect on the critical buckling load for different temperature differences

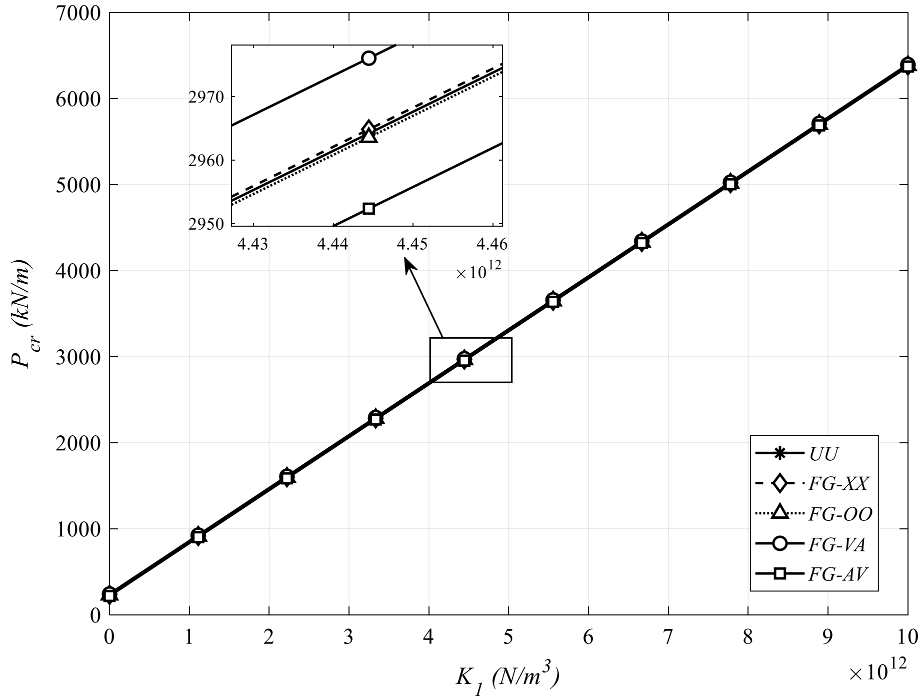

Fig. 15 Influence of springs' parameter on the critical buckling load for various types of CNTs' dispersion

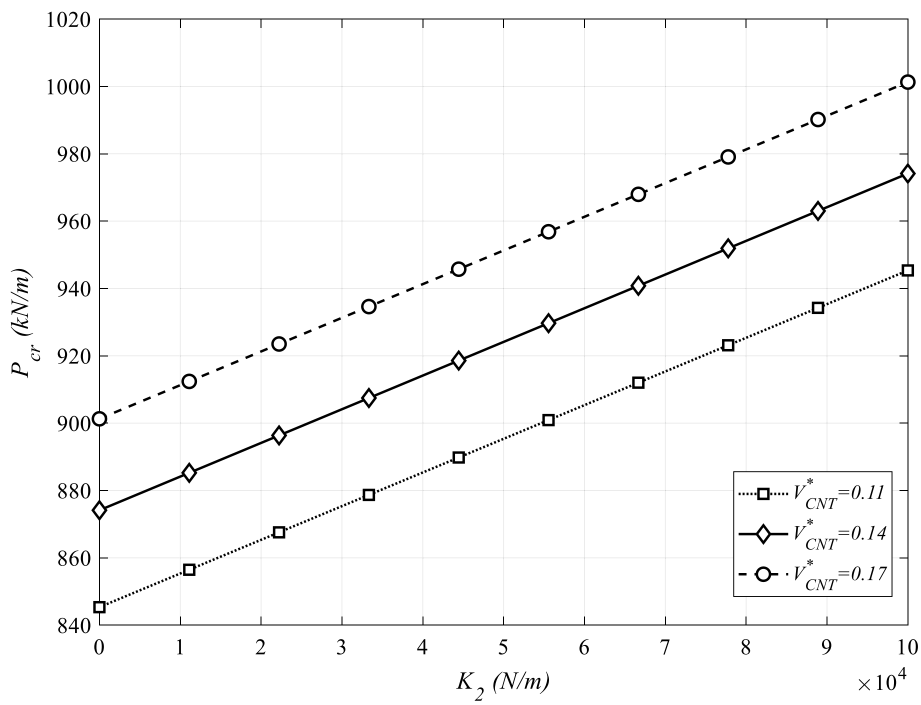

Fig. 16 Shear layer's parameter variations effect on the critical buckling load

6 Conclusions

Free vibration and mechanical buckling responses of a three-layered curved microbeam were investigated under a longitudinal Lorentz magnetic load. The influence of a thermal environment was also considered on the mechanical behaviors of the structure. The core was made from FG porous materials whose properties vary through the thickness direction based on three patterns. The faces were composed of FG-CNTRCs and the impact of the placement of CNTs on the face properties was considered. Using ERM, the effective thermo-mechanical properties of the nanocomposite face sheets were also

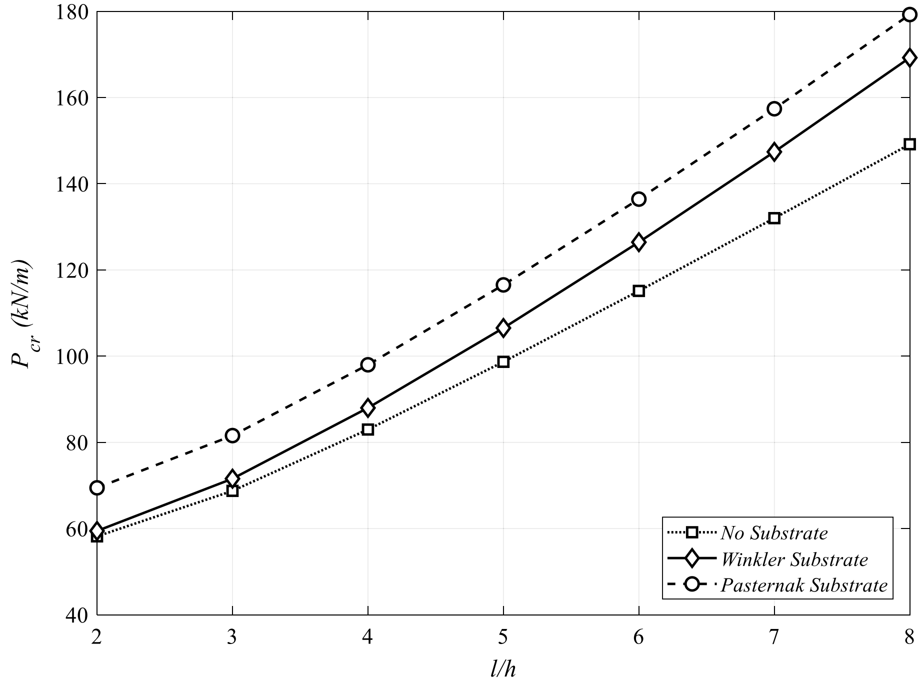

Fig. 17 Size effect on the critical buckling load of the micro structure for different kinds of substrate

explored. Since this work analyzed the small-dimension structures, MCST was used to predict the results on the micro-scale. The kinematic relations were derived based on HSDT and using von Karman's assumptions. The variational approach and energy method were used to derive the governing equations which were analytically solved for both simply supported ends via Navier's solution method. The results in both vibrational and buckling domains were verified with the previously published reports on simpler states and the effects of various parameters on the results were considered. The chief conclusions are:

- Since increasing the porosity coefficient caused a reduction in stiffness of the structure, its enhancement will reduce both natural frequency and critical buckling load of the microstructure.
- Among the three considered types of porosity distribution, types B and C led to the maximum and minimum values of frequency and critical buckling load, respectively. Type B was related to symmetric pore pattern while type C reflected uniform pattern.
- Increasing the number of CNTs in the faces enhanced their stiffness, and accordingly, raised the natural frequency and critical buckling load.
- Comparing different patterns of CNTs' dispersion, it was found that FG-VA and FG-AV resulted in the highest and lowest natural frequency and critical buckling load, respectively.
- Regarding higher stiffness of the face sheets than the core, an increment in the core thickness, at the constant total thickness, may decrement the stiffness of the structure; thus, both natural frequency and critical buckling load will be declined.
- Keeping the curvature radius constant and by increasing the central opening angle, the natural frequency and critical buckling load were enhanced.
- As the intensity of the applied longitudinal magnetic field increased, the natural frequency and critical buckling load were enhanced.
- Increasing the dimensionless length-scale parameter (h/l) declined the results.
- Regardless of its type inclusion of an elastic substrate incremented both frequency and critical buckling load.
- While increasing springs and shear layer parameters enhanced the results, an enhancement in the dashpots parameter declined them.

Acknowledgements The authors would like to thank the reviewers for their valuable comments and suggestions to improve the clarity of this study.

Funding The authors are thankful to the University of Kashan for supporting this work by Grant No. 988099/3.

Compliance with ethical standards

Conflict of interest The authors declare no conflict of interests.

Appendix

The non-zero components of stiffness, damping, and mass matrices in Eq. (49) can be defined as:

$$K_{11} = Q_{110}\Xi^2 + \frac{Q_{550}}{R^2} + \frac{l^2\beta_1\Xi^2}{8R^2},$$

$$K_{12} = -Q_{111}\Xi^3 - \frac{Q_{110}\Xi}{R} - \frac{Q_{551}\Xi}{R^2} - \frac{l^2\beta_1\Xi^3}{4R} - \frac{l^2\beta_2\Xi^3}{8R^2},$$

$$K_{13} = Q_{113}\Xi^2 - \frac{Q_{556}}{R} + \frac{Q_{553}}{R^2} + \frac{l^2\beta_7\Xi^2}{8R} + \frac{l^2\beta_4\Xi^2}{8R^2},$$

$$K_{21} = -Q_{111}\Xi^3 - \frac{Q_{110}\Xi}{R} - \frac{Q_{551}\Xi}{R^2} - \frac{l^2\beta_1\Xi^3}{4R} - \frac{l^2\beta_2\Xi^3}{8R^2},$$

$$K_{22} = \frac{Q_{110}}{R^2} + Q_{112}\Xi^4 - N_T\Xi^2 - N_0\Xi^2 - K_2\Xi^2 - K_1 + \frac{Q_{552}\Xi^2}{R^2} - \eta H_x^2\Xi^2 + 2\frac{Q_{111}\Xi^2}{R} + \frac{1}{2}l^2\beta_1\Xi^4 + \frac{l^2\beta_1\Xi^2}{8R^2} + \frac{l^2\beta_2\Xi^4}{2R} + \frac{l^2\beta_3\Xi^4}{8R^2},$$

$$K_{23} = -Q_{115}\Xi^3 - \frac{Q_{113}\Xi}{R} + \frac{Q_{557}\Xi}{R} - \frac{Q_{555}\Xi}{R^2} - \frac{1}{4}l^2\beta_7\Xi^3 - \frac{l^2\beta_6\Xi^3}{8R^2} - \frac{l^2\beta_{11}\Xi}{8R} - \frac{l^2\beta_7\Xi}{8R^2} - \frac{l^2\beta_4\Xi^3}{4R} - \frac{l^2\beta_8\Xi^3}{8R},$$

$$K_{31} = Q_{113}\Xi^2 - \frac{Q_{556}}{R} + \frac{Q_{553}}{R^2} + \frac{l^2\beta_7\Xi^2}{8R} + \frac{l^2\beta_4\Xi^2}{8R^2},$$

$$K_{32} = -Q_{115}\Xi^3 + \frac{Q_{557}\Xi}{R} - \frac{1}{4}l^2\beta_7\Xi^3 - \frac{Q_{555}\Xi}{R^2} - \frac{Q_{113}\Xi}{R} - \frac{l^2\beta_4\Xi^3}{4R} - \frac{l^2\beta_6\Xi^3}{8R^2} + \frac{l^2\beta_7\Xi}{8R^2} - \frac{l^2\beta_8\Xi^3}{8R} - \frac{l^2\beta_{11}\Xi}{8R},$$

$$K_{33} = Q_{559} + \frac{1}{8}l^2\beta_{13} + \frac{Q_{554}}{R^2} + Q_{114}\Xi^2 - 2\frac{Q_{558}}{R} - \frac{l^2\beta_{10}}{8R^2} + \frac{1}{8}l^2\beta_{10}\Xi^2 + \frac{l^2\beta_5\Xi^2}{8R^2} + \frac{l^2\beta_9\Xi^2}{4R},$$

$$M_{11} = -I_0, \qquad M_{12} = I_1\Xi, \qquad M_{13} = -I_3,$$

$$M_{21} = I_1\Xi, \qquad M_{22} = -I_0 - I_2\Xi^2, \qquad M_{23} = I_5\Xi,$$

$$M_{31} = -I_3, \qquad M_{32} = I_5\Xi, \qquad M_{33} = -I_4,$$

$$C_{22} = -D$$

References

1. McEvoy MA, Correll N. Materials that couple sensing, actuation, computation, and communication. Sci (80) Am Assoc Adv Sci. 2015;347:1261689.
2. Mohammadimehr M, Arshid E, Alhosseini SMAR, Amir S, Arani MRG. Free vibration analysis of thick cylindrical MEE composite shells reinforced CNTs with temperature-dependent properties resting on viscoelastic foundation. Struct Eng Mech. 2019;70:683–702.
3. Iijima S. Helical microtubules of graphitic carbon. Nature. Nature Publishing Group; 1991;354:56.
4. Ajayan PM, Zhou OZ. Applications of carbon nanotubes. Carbon nanotube. Berlin, Heidelberg: Springer, Berlin, Heidelberg; 2001. p. 391–425. http://link.springer.com/https://doi.org/10.1007/3-540-39947-X_14
5. Anumandla V, Gibson RF. A comprehensive closed form micromechanics model for estimating the elastic modulus of nanotube-reinforced composites. Compos Part A Appl Sci Manuf. Elsevier; 2006;37:2178–85. https://www.sciencedirect.com/science/article/pii/S1359835X05003830
6. Thostenson ET, Chou T-W. On the elastic properties of carbon nanotube-based composites: modelling and characterization. J Phys D Appl Phys. IOP Publishing; 2003;36:573.
7. Alibeigloo A. Static analysis of functionally graded carbon nanotube-reinforced composite plate embedded in piezoelectric layers by using theory of elasticity. Compos Struct Elsevier. 2013;95:612–22.
8. Duc ND, Cong PH, Tuan ND, Tran P, Thanh N Van. Thermal and mechanical stability of functionally graded carbon nanotubes (FG CNT)-reinforced composite truncated conical shells surrounded by the elastic foundations. Thin-Walled Struct. Elsevier; 2017;115:300–10. https://www.sciencedirect.com/science/article/pii/S0263823116307467
9. Shariati A, Ghabussi A, Habibi M, Safarpour H, Safarpour M, Tounsi A, et al. Extremely large oscillation and nonlinear frequency of a multi-scale hybrid disk resting on nonlinear elastic foundation. Thin-Walled Struct. Elsevier Ltd; 2020;154:106840.
10. Khatua TP, Cheung YK. Bending and vibration of multilayer sandwich beams and plates. Int J Numer Methods Eng. 1973;6:11–24.
11. Maheri MR, Adams RD. Steady-state flexural vibration damping of honeycomb sandwich beams. Compos Sci Technol Elsevier. 1994;52:333–47.
12. Leclaire P, Horoshenkov KV, Cummings A. Transverse vibrations of a thin rectangular porous plate saturated by a fluid. J Sound Vib. 2001;247:1–18. http://linkinghub.elsevier.com/retrieve/pii/S0022460X01936569
13. Takahashi D, Tanaka M. Flexural vibration of perforated plates and porous elastic materials under acoustic loading. J Acoust Soc Am. Acoustical Society of America; 2002;112:1456–64. http://asa.scitation.org/doi/https://doi.org/10.1121/1.1497624
14. Chen D, Yang J, Kitipornchai S. Elastic buckling and static bending of shear deformable functionally graded porous beam. Compos Struct. Elsevier; 2015;133:54–61. https://www.sciencedirect.com/science/article/pii/S0263822315005978

15. Guo Y, Zhang J. Shock absorbing characteristics and vibration transmissibility of honeycomb paperboard. Shock Vib. 2004;11:521–31.
16. Ait AH, Tounsi A, Bernard F. Effect of thickness stretching and porosity on mechanical response of a functionally graded beams resting on elastic foundations. Int J Mech Mater Des. Springer Netherlands; 2017;13:71–84. http://link.springer.com/https://doi.org/10.1007/s10999-015-9318-x
17. Chen D, Yang J, Kitipornchai S. Free and forced vibrations of shear deformable functionally graded porous beams. Int J Mech Sci. Elsevier; 2016;108–109:14–22. https://www.sciencedirect.com/science/article/pii/S002074031600031X
18. Katunin A. Vibration-based spatial damage identification in honeycomb-core sandwich composite structures using wavelet analysis. Compos Struct. 2014;118:385–91.
19. Chen D, Yang J, Kitipornchai S. Nonlinear vibration and postbuckling of functionally graded graphene reinforced porous nanocomposite beams. Compos Sci Technol. Elsevier; 2017;142:235–45. https://www.sciencedirect.com/science/article/abs/pii/S0266353816320383
20. Duc ND, Seung-Eock K, Tuan ND, Tran P, Khoa ND. New approach to study nonlinear dynamic response and vibration of sandwich composite cylindrical panels with auxetic honeycomb core layer. Aerosp Sci Technol. 2017;70:396–404.
21. Amir S, Khorasani M, BabaAkbar-Zarei H. Buckling analysis of nanocomposite sandwich plates with piezoelectric face sheets based on flexoelectricity and first-order shear deformation theory. J Sandw Struct Mater. SAGE PublicationsSage UK: London, England; 2018;109963621879538. http://journals.sagepub.com/doi/https://doi.org/10.1177/1099636218795385
22. Amir S, BabaAkbar-Zarei H, Khorasani M. Flexoelectric vibration analysis of nanocomposite sandwich plates. Mech Based Des Struct Mach. Taylor & Francis; 2020;48:146–63. https://www.tandfonline.com/doi/full/https://doi.org/10.1080/15397734.2019.1624175
23. Piollet E, Fotsing ER, Ross A, Michon G. High damping and nonlinear vibration of sandwich beams with entangled cross-linked fibres as core material. Compos Part B Eng. 2019;168:353–66.
24. Shariati A, Habibi M, Tounsi A, Safarpour H, Safa M. Application of exact continuum size-dependent theory for stability and frequency analysis of a curved cantilevered microtubule by considering viscoelastic properties. Eng Comput. Springer; 2020;1–20. https://link.springer.com/article/https://doi.org/10.1007/s00366-020-01024-9
25. Babaei H, Eslami MR, Khorshidvand AR. Thermal buckling and postbuckling responses of geometrically imperfect FG porous beams based on physical neutral plane. J Therm Stress. 2020;43:109–31.
26. Kumar S, Renji K. Estimation of strains in composite honeycomb sandwich panels subjected to low frequency diffused acoustic field. J Sound Vib. 2019;449:84–97.
27. Moayedi H, Habibi M, Safarpour H, Safarpour M, Foong LK. Buckling and frequency responses of a graphene nanoplatelet reinforced composite microdisk. Singapore: World Scientific Publishing Co. Pte Ltd; 2019. p. 11.
28. Amir S, Arshid E, Ghorbanpour AMR. Size-dependent magneto-electro-elastic vibration analysis of FG saturated porous annular/circular micro sandwich plates embedded with nanocomposite face sheets subjected to multi-physical pre loads. Smart Struct Syst. 2019;23:429–47. https://doi.org/10.12989/sss.2019.23.5.429.
29. Eringen AC. On differential equations of nonlocal elasticity and solutions of screw dislocation and surface waves. J Appl Phys AIP. 1983;54:4703–10.
30. Eringen AC. Nonlocal continuum field theories. Berlin: Springer Science and Business Media; 2002.
31. Amir S, Soleimani-Javid Z, Arshid E. Size-dependent free vibration of sandwich micro beam with porous core subjected to thermal load based on SSDBT. ZAMM Zeitschrift fur Angew Math und Mech. 2019;99:1–21.
32. Amir S, Bidgoli EMR, Arshid E. Size-dependent vibration analysis of a three-layered porous rectangular nano plate with piezo-electromagnetic face sheets subjected to pre loads based on SSDT. Mech Adv Mater Struct. Taylor & Francis; 2020;27:605–19. https://www.tandfonline.com/doi/full/https://doi.org/10.1080/15376494.2018.1487612
33. Allahkarami F, Nikkhah-Bahrami M. The effects of agglomerated CNTs as reinforcement on the size-dependent vibration of embedded curved microbeams based on modified couple stress theory. Mech Adv Mater Struct. Taylor and Francis Inc.; 2018;25:995–1008.
34. Alipour MM, Shariyat M. Nonlocal zigzag analytical solution for Laplacian hygrothermal stress analysis of annular sandwich macro/nanoplates with poor adhesions and 2D-FGM porous cores. Arch Civ Mech Eng. Elsevier B.V.; 2019;19:1211–34.
35. Yi H, Sahmani S, Safaei B. On size-dependent large-amplitude free oscillations of FGPM nanoshells incorporating vibrational mode interactions. Arch Civ Mech Eng Springer. 2020;20:1–23.
36. Safarpour H, Esmailpoor HZ, Habibi M. A size-dependent exact theory for thermal buckling, free and forced vibration analysis of temperature dependent FG multilayer GPLRC composite nanostructures restring on elastic foundation. Int J Mech Mater Des. Springer Netherlands; 2019;15:569–83. https://link.springer.com/article/https://doi.org/10.1007/s10999-018-9431-8
37. Esmailpoor HZ, Pourghader J, Hashemabadi D, Sharifi BF, Habibi M, Safarpour H. Multilayer GPLRC composite cylindrical nanoshell using modified strain gradient theory. Mech Based Des Struct Mach. Taylor and Francis Inc.; 2019;47:521–45.
38. Sobhy M. Differential quadrature method for magneto-hygrothermal bending of functionally graded graphene/Al sandwich-curved beams with honeycomb core via a new higher-order theory. J Sandw Struct Mater. 2020
39. Lei YL, Gao K, Wang X, Yang J. Dynamic behaviors of single- and multi-span functionally graded porous beams with flexible boundary constraints. Appl Math Model. 2020;83:754–76.
40. Bidgoli MO, Arefi M, Loghman A. Thermoelastic behaviour of FGM rotating cylinder resting on friction bed subjected to a thermal gradient and an external torque. Aust J Mech Eng. Taylor and Francis Ltd.; 2018; https://www.tandfonline.com/doi/abs/https://doi.org/10.1080/14484846.2018.1552736
41. Mahani RB, Eyvazian A, Musharavati F, Sebaey TA, Talebizadehsardari P. Thermal buckling of laminated nano-composite conical shell reinforced with graphene platelets. Thin-Walled Struct. Elsevier Ltd; 2020;155:106913.
42. Arshid E, Amir S, Loghman A. Bending and buckling behaviors of heterogeneous temperature-dependent micro annular/circular porous sandwich plates integrated by FGPEM nano-Composite layers. J Sandw Struct Mater. SAGE PublicationsSage UK: London, England; 2020;109963622095502. http://journals.sagepub.com/doi/https://doi.org/10.1177/1099636220955027
43. Bousahla AA, Bourada F, Mahmoud SR, Tounsi A, Algarni A, Adda Bedia EA, et al. Buckling and dynamic behavior of the simply supported CNT-RC beams using an integral-first shear deformation theory. Comput Concr Techno Press. 2020;25:155–66.
44. Refrafi S, Bousahla AA, Bouhadra A, Menasria A, Bourada F, Tounsi A, et al. Effects of hygro-thermo-mechanical conditions on the buckling of FG sandwich plates resting on elastic foundations. Comput Concr Techno Press. 2020;25:311–25.
45. Chikr SC, Kaci A, Bousahla AA, Bourada F, Tounsi A, Bedia EA, et al. A novel four-unknown integral model for buckling response of FG sandwich plates resting on elastic foundations under various

boundary conditions using Galerkin's approach. Geomech Eng Techno-Press. 2020;21:471–87.
46. Dinh DN, Hong CP. Nonlinear thermo-mechanical dynamic analysis and vibration of higher order shear deformable piezoelectric functionally graded material sandwich plates resting on elastic foundations. J Sandw Struct Mater. SAGE PublicationsSage UK: London, England; 2018;20:191–218. http://journals.sagepub.com/doi/https://doi.org/10.1177/1099636216648488
47. Zenkour AM. A quasi-3D refined theory for functionally graded single-layered and sandwich plates with porosities. Compos Struct. Elsevier; 2018;201:38–48. https://www.sciencedirect.com/science/article/pii/S026382231831420X
48. Arshid E, Khorshidvand AR. Free vibration analysis of saturated porous FG circular plates integrated with piezoelectric actuators via differential quadrature method. Thin-Walled Struct Elsevier Ltd. 2018;125:220–33. https://doi.org/10.1016/j.tws.2018.01.007.
49. Chen D, Yang J, Kitipornchai S. Buckling and bending analyses of a novel functionally graded porous plate using Chebyshev-Ritz method. Arch Civ Mech Eng. Elsevier; 2019;19:157–70. https://www.sciencedirect.com/science/article/pii/S1644966518301158
50. Zenkour AM, Aljadani MH. Porosity effect on thermal buckling behavior of actuated functionally graded piezoelectric nanoplates. Eur J Mech A/Solids. Elsevier Ltd; 2019;78:103835.
51. Arshid E, Khorshidvand AR, Khorsandijou SM. The effect of porosity on free vibration of SPFG circular plates resting on visco-Pasternak elastic foundation based on CPT, FSDT and TSDT. Struct Eng Mech. 2019;70:97–112. http://dx.doi.org/https://doi.org/10.12989/sem.2019.70.1.097
52. Pourjabari A, Hajilak ZE, Mohammadi A, Habibi M, Safarpour H. Effect of Porosity on free and forced vibration characteristics of the GPL reinforcement composite nanostructures. Comput Math with Appl Elsevier Ltd. 2019;77:2608–26.
53. Amir S, Arshid E, Rasti-Alhosseini SMA, Loghman A. Quasi-3D tangential shear deformation theory for size-dependent free vibration analysis of three-layered FG porous micro rectangular plate integrated by nano-composite faces in hygrothermal environment. J Therm Stress. Taylor & Francis; 2020;43:133–56. https://www.tandfonline.com/doi/full/https://doi.org/10.1080/01495739.2019.1660601
54. Ansari R, Torabi J, Shojaei MF. Buckling and vibration analysis of embedded functionally graded carbon nanotube-reinforced composite annular sector plates under thermal loading. Compos Part B Eng. Elsevier; 2017;109:197–213. https://www.sciencedirect.com/science/article/abs/pii/S1359836816313907
55. Ghorbanpour AA, Haghparast E, BabaAkbar ZH. Vibration characteristics of axially moving titanium- polymer nanocomposite faced sandwich plate under initial tension. Int J Eng Appl Sci. 2017;9:39–39. http://dergipark.gov.tr/doi/https://doi.org/10.24107/ijeas.303299
56. Ansari R, Torabi J, Hosein Shakouri A. Vibration analysis of functionally graded carbon nanotube-reinforced composite elliptical plates using a numerical strategy. Aerosp Sci Technol. Elsevier Masson; 2017;60:152–61. https://www.sciencedirect.com/science/article/pii/S1270963816303613
57. Liu YP, Reddy JN. A nonlocal curved beam model based on a modified couple stress theory. Int J Struct Stab Dyn. 2011;11:495–512.
58. Şimşek M, Reddy JN. Bending and vibration of functionally graded microbeams using a new higher order beam theory and the modified couple stress theory. Int J Eng Sci. 2013;64:37–53.
59. Thai CH, Ferreira AJM, Phung-Van P. Size dependent free vibration analysis of multilayer functionally graded GPLRC microplates based on modified strain gradient theory. Compos Part B Eng Elsevier Ltd. 2019;169:174–88.
60. Soleimani I, Beni YT. Vibration analysis of nanotubes based on two-node size dependent axisymmetric shell element. Arch Civ Mech Eng. Elsevier B.V.; 2018;18:1345–58.
61. Arshid E, Amir S, Loghman A. Static and dynamic analyses of FG-GNPs reinforced porous nanocomposite annular micro-plates based on MSGT. Int J Mech Sci. Elsevier Ltd; 2020;180:105656. https://linkinghub.elsevier.com/retrieve/pii/S0020740320302678
62. Amir S, Arshid E, Khoddami MZ, Loghman A, Ghorbanpour AA. Vibration analysis of magnetorheological fluid circular sandwich plates with magnetostrictive facesheets exposed to monotonic magnetic field located on visco-Pasternak substrate. JVC/J Vib Control. 2020;26:1523–37. https://doi.org/10.1177/1077546319899203
63. Arshid E, Kiani A, Amir S. Magneto-electro-elastic vibration of moderately thick FG annular plates subjected to multi physical loads in thermal environment using GDQ method by considering neutral surface. Proc Inst Mech Eng Part L J Mater Des Appl. 2019;233:2140–59. https://doi.org/10.1177/1464420719832626.
64. Zenkour AM, Radwan AF. Compressive study of functionally graded plates resting on Winkler–Pasternak foundations under various boundary conditions using hyperbolic shear deformation theory. Arch Civ Mech Eng. Elsevier B.V.; 2018;18:645–58.
65. Mekerbi M, Benyoucef S, Mahmoudi A, Tounsi A, Bousahla AA, Mahmoud SR. Thermodynamic behavior of functionally graded sandwich plates resting on different elastic foundation and with various boundary conditions. J Sandw Struct Mater. SAGE PublicationsSage UK: London, England; 2019;109963621985128. http://journals.sagepub.com/doi/https://doi.org/10.1177/1099636219851281
66. Sahmani S, Aghdam MM. Imperfection sensitivity of the size-dependent postbuckling response of pressurized FGM nanoshells in thermal environments. Arch Civ Mech Eng. Elsevier B.V.; 2017;17:623–38.
67. Behravan RA, Shariyat M. Thermo-magneto-elasticity analysis of variable thickness annular FGM plates with asymmetric shear and normal loads and non-uniform elastic foundations. Arch Civ Mech Eng. Elsevier B.V.; 2016;16:448–66.
68. Rezvani SS, Kiasat MS. Analytical and experimental investigation on the free vibration of a floating composite sandwich plate having viscoelastic core. Arch Civ Mech Eng. Elsevier B.V.; 2018;18:1241–58.
69. Ansari R, Gholami R, Sahmani S. Free vibration analysis of size-dependent functionally graded microbeams based on the strain gradient Timoshenko beam theory. Compos Struct Elsevier Ltd. 2011;94:221–8. https://doi.org/10.1016/j.compstruct.2011.06.024.
70. Ma HM, Gao XL, Reddy JN. A microstructure-dependent Timoshenko beam model based on a modified couple stress theory. J Mech Phys Solids. 2008;56:3379–91.
71. Zhang B, He Y, Liu D, Gan Z, Shen L. A novel size-dependent functionally graded curved mircobeam model based on the strain gradient elasticity theory. Compos Struct Elsevier. 2013;106:374–92.
72. Allahkarami F, Nikkhah-bahrami M, Saryazdi MG. Magneto-thermo-mechanical dynamic buckling analysis of a FG-CNTs-reinforced curved microbeam with different boundary conditions using strain gradient theory. Int J Mech Mater Des. Springer Netherlands; 2018;14:243–61.
73. Shen H-S. Postbuckling of nanotube-reinforced composite cylindrical shells in thermal environments, Part I: axially-loaded shells. Compos Struct Elsevier. 2011;93:2096–108.
74. Reddy JN. Nonlocal theories for bending, buckling and vibration of beams. Int J Eng Sci. 2007;45:288–307.
75. Aydogdu M. A general nonlocal beam theory: Its application to nanobeam bending, buckling and vibration. Phys E

Low-Dimens Syst Nanostruct Elsevier. 2009;41:1651–5. https://doi.org/10.1016/j.physe.2009.05.014.

76. Eltaher MA, Emam SA, Mahmoud FF. Static and stability analysis of nonlocal functionally graded nanobeams. Compos Struct Elsevier Ltd. 2013;96:82–8. https://doi.org/10.1016/j.compstruct.2012.09.030.